International Journal of Mechanical Sciences 329 (2026) 112110

Contents lists available at ScienceDirect

International Journal of Mechanical Sciences

journal homepage: www.elsevier.com/locate/ijmecsci

Machine learning-enabled inverse design of heterogeneous impact-resistant metamaterials

Shitong Fang [a], Haobin Lin [a], Aipeng Ye [a], Zhihui Lai [a], Haitao Ye [b], Qiang Gao [c], Mingjing Cai [d], Xiaoya Zhai [e], Xiaohao Sun [f], Liuchao Jin [b,*], Wei-Hsin Liao [b,g,*]

[a] National Key Laboratory of Green and Long-Life Road Engineering in Extreme Environment (Shenzhen), Shenzhen University, Shenzhen, 518051, China
[b] Department of Mechanical and Automation Engineering, The Chinese University of Hong Kong, Hong Kong Special Administrative Region of China
[c] School of Mechanical Engineering, Southeast University, Nanjing, PR China
[d] Guangzhou Institute of Technology and School of Mechano-Electronic Engineering, Xidian University, Guangzhou, China
[e] School of Mathematical Sciences, University of Science and Technology of China, Hefei, 230027, China
[f] CAS Key Laboratory of Mechanical Behavior and Design of Materials, Department of Modern Mechanics, University of Science and Technology of China, Hefei, 230027, China
[g] Institute of Intelligent Design and Manufacturing, The Chinese University of Hong Kong, Hong Kong Special Administrative Region of China

ARTICLE INFO

Keywords:
Mechanical metamaterials
Machine learning
Inverse design
Heterogeneous multi-material lattices
Energy absorption
Impact mitigation

ABSTRACT

Designing impact-resistant responses in heterogeneous multi-material metamaterials remains challenging because the discrete material-layout space is high-dimensional and non-intuitive, particularly when specific energy absorption (SEA) must be increased without amplifying the peak impact force in applications such as unmanned aerial vehicle (UAV) airdrop. Despite recent advances in inverse design, data-driven optimization of impact response remains constrained by the scarcity of high-fidelity datasets that jointly represent dynamic loading and material failure. This study develops a machine-learning-enabled inverse-design framework for non-periodic heterogeneous multi-material metamaterials using a fracture-aware finite-element dataset generated under quasi-static compression and dynamic impact. A ductile damage model is used to represent polylactic acid (PLA) failure, and a Transformer-based surrogate learns the mapping from cell-wise PLA/thermoplastic polyurethane (TPU) layouts to the stress–strain response and peak impact force. The surrogate is coupled with the non-dominated sorting genetic algorithm II (NSGA-II) to identify Pareto-optimal designs in the combinatorial layout space. Across comparable designs, the optimized layouts achieved up to 58% higher SEA and 47.4% lower peak force, and the predicted improvements were verified by quasi-static compression and drop-weight impact tests. In UAV airdrop experiments, the optimized design produced a payload-acceleration peak comparable to that of pure TPU while avoiding the pronounced rebound and overturning observed for the compliant single-material box. These results demonstrate that spatially heterogeneous multi-material layouts can balance energy absorption, force attenuation, and post-impact stability.

1. Introduction

Mechanical metamaterials, enabled by the deliberate design of microstructural geometry and spatial architecture, can exhibit mechanical responses that are difficult to achieve in conventional homogeneous materials, making them promising candidates for impact-protection applications [1–5]. Effective impact protection requires a structure to absorb and dissipate the incident energy within the available deformation stroke while limiting the force transmitted to the protected object. Increasing stiffness or the sustained crushing load can improve energy-absorption capacity but commonly produces a higher transmitted force, whereas a more compliant response can suppress the force peak but may provide insufficient load-bearing capacity or exhaust the available stroke before the required energy has been dissipated [6–11]. Conventional absorbers, such as homogeneous foams and periodic honeycombs, offer limited freedom to regulate these two aspects independently because their responses are governed by a fixed material composition and prescribed cell geometry [12–21]. Recent mechanical-sciences studies have advanced impact-resistant origami and hybrid honeycomb–chiral architectures, quasi-zero-stiffness systems, and pre-torsion tubular lattices, demonstrating how localization control, multidirectional energy absorption, vibration–impact coupling,

* Corresponding authors.
E-mail addresses: Liuchao.Jin@link.cuhk.edu.hk (L. Jin), whliao@cuhk.edu.hk (W.-H. Liao).

https://doi.org/10.1016/j.ijmecsci.2026.112110
Received 17 June 2026; Received in revised form 5 September 2026; Accepted 10 September 2026
Available online 16 September 2026

and geometry-induced deformation pathways can broaden protective functionality [22–25]. However, these approaches predominantly tune geometric mechanisms within prescribed material architectures and therefore do not resolve the structural-scale material-assignment problem considered here. In the present study, energy-absorption performance is quantified by SEA, whereas impact-force attenuation is characterized by the peak impact force [26,27]. This fundamental competition between energy-absorption capacity and impact-force attenuation motivates the development of heterogeneous metamaterials with programmable spatial material distributions [28–35].

To overcome the performance ceiling of conventional single-material structures, researchers have sought to replace portions of the stiff constituents in metamaterials, such as honeycomb and chiral architectures, with soft polymers or other materials with distinct mechanical properties, aiming to regulate deformation and energy absorption [28–30,36–39]. However, such approaches are frequently limited by predefined material zoning patterns and low-dimensional scans over a few geometric parameters, making it difficult to achieve systematic control in a higher-dimensional material-layout space [40–43]. Studies indicate that introducing soft–hard composites can activate multiple dissipation mechanisms through inter-phase synergy: the soft phase accommodates large deformation and reconfiguration for energy dissipation, while the hard phase provides load-bearing capacity and constraints that reshape load-transfer pathways [44–47]. Typically, substituting selected beam members within a unit cell with a softer material can promote preferential buckling of soft beams and trigger negative stiffness or multistable plateaus [48,49], thereby enabling smoother load evolution and higher energy-absorption efficiency. Related efforts have explored this mechanism across different structural levels and implementation strategies. For example, geometric constraints such as compliant arches and hinges have been incorporated into beam members to reduce local bending and enhance global stability [44,45], yielding more controllable plastic evolution and tunable responses. Other studies have constructed composite negative-stiffness or multi-material negative-stiffness units [48,50–53] to realize reusable cushioning and energy-absorbing behavior, outperforming single-material counterparts in metrics such as compressive strength and volumetric energy absorption. At the honeycomb/lattice scale, soft–hard coupling can further induce staged collapses with multiple stress plateaus, extending the effective stroke for energy absorption and improving plateau stability [54,55]. Recent dual-phase studies further show that hierarchical phase organization and reusable phase-transition-enabled honeycombs can regulate the deformation sequence and sustained load [56,57]. These findings reinforce the importance of phase interaction, while their rule-defined topologies leave open the systematic search of non-periodic discrete assignments. Despite these advances demonstrating the potential of soft–hard composites for energy absorption, current multi-material energy-absorbing metamaterial designs remain largely driven by experience-based configuration assumptions or limited parametric studies. Material layouts are often prescribed as regular gradients or periodic patterns/partitions [40,41,58], which severely restrict the systematic exploration of high-dimensional material-distribution spaces and hinder the realization of truly programmable macroscopic responses and further improvements in energy-absorption performance.

Against this background, inverse-design and optimization methodologies for metamaterials have rapidly evolved in recent years, enabling a transition from experience-driven configuration presets to computable and searchable high-dimensional design spaces [59–65]. Recent studies have also used generative deep learning to program irregular nonlinear responses and ensemble learning to decouple hybrid-metamaterial objectives [66,67]. These advances demonstrate the growing capability of data-driven design, but they do not simultaneously address fracture-aware quasi-static and impact responses for structural-scale multi-material layouts. In this context, researchers commonly use the unit cell as the fundamental design entity, treating the assignment of soft/hard materials or the microstructural morphology within the cell as design variables. After imposing constraints such as material volume fraction, existing studies have employed machine learning, topology optimization, and evolutionary algorithms to tune effective mechanical properties toward target responses [68–76]. The machine-learning-driven hierarchical composite design framework proposed by Gu et al. which combines simulation databases with additive manufacturing experiments, demonstrates an efficient pathway for exploring high-dimensional structural spaces [68]. Furthermore, Pahlavani et al. introduced deep learning to identify “rare-event” designs for random hard/soft assignments in regular lattices and validated them via multi-material 3D printing, highlighting the feasibility of establishing a “material layout–mechanical property” mapping in a vast discrete assignment space [69]. Zhang et al. developed an approach based on independent point density interpolation (iPDI) and a multi-material model to optimize periodic unit-cell topology under soft–hard volume constraints, aiming to minimize Poisson’s ratio while computing effective elastic properties [70]. Li et al. through combined computational and experimental investigations, systematically revealed the decisive role of multi-material spatial configurations in the macroscopic stiffness–toughness balance, further confirming the critical impact of unit-cell-scale material distribution [77,78]. Nevertheless, although substantial progress has been made on unit-cell-scale multi-material assignment and property optimization, existing studies still predominantly focus on periodic unit-cell construction and effective-property tuning [69–71]. Systematic inverse design of multi-material layouts at the lattice scale remains relatively scarce, especially work that treats non-periodic, discrete material assignment at the structural scale as the core design variable and targets joint optimization of SEA and peak impact force. Therefore, for practical impact-protection scenarios, it is urgent to establish a unified design framework that can freely explore material assignment in non-periodic lattice structures and directly perform joint multi-objective optimization and inverse design for SEA and peak impact force [79–89].

Lightweight impact-protective structures are required in UAV-based emergency delivery and urban last-mile logistics, where fragile payloads may experience direct ground impact or buffered landing [90,91] (Fig. 1a,b). To address the associated design challenge, a fracture-aware, machine-learning-enabled inverse-design framework is established to search structural-scale PLA/TPU assignments within a fixed re-entrant lattice (Fig. 1c). Each candidate design is represented by a 4×7 binary matrix specifying the cell-wise material arrangement, while progressive PLA damage is retained during dataset generation and design evaluation. Fracture-aware finite-element simulations are performed under quasi-static compression and 5 J impact loading to obtain the nominal stress–strain response, SEA, force–time response, and peak impact force. A Transformer-based dual-response surrogate is trained to predict these responses and is subsequently coupled with NSGA-II to identify Pareto-optimal layouts that maximize SEA while minimizing peak impact force. Representative designs are examined to determine how soft-phase connectivity and hard-phase skeleton continuity govern the balance between energy absorption and impact-force attenuation. The selected layouts are subsequently evaluated through compression, drop-weight impact, and UAV airdrop experiments to assess their predicted mechanical performance and practical protective capability.

The principal contributions of this study are threefold. First, an application-driven structural-scale heterogeneous material-layout strategy is developed for UAV impact protection. PLA and TPU are independently assigned across 28 cells of a fixed re-entrant structure, enabling non-periodic material organization to be explored at the structural scale. UAV airdrop experiments further demonstrate that the minimum instantaneous acceleration does not necessarily correspond to the best protection because rebound and post-impact stability must also be considered. Second, progressive PLA failure is incorporated

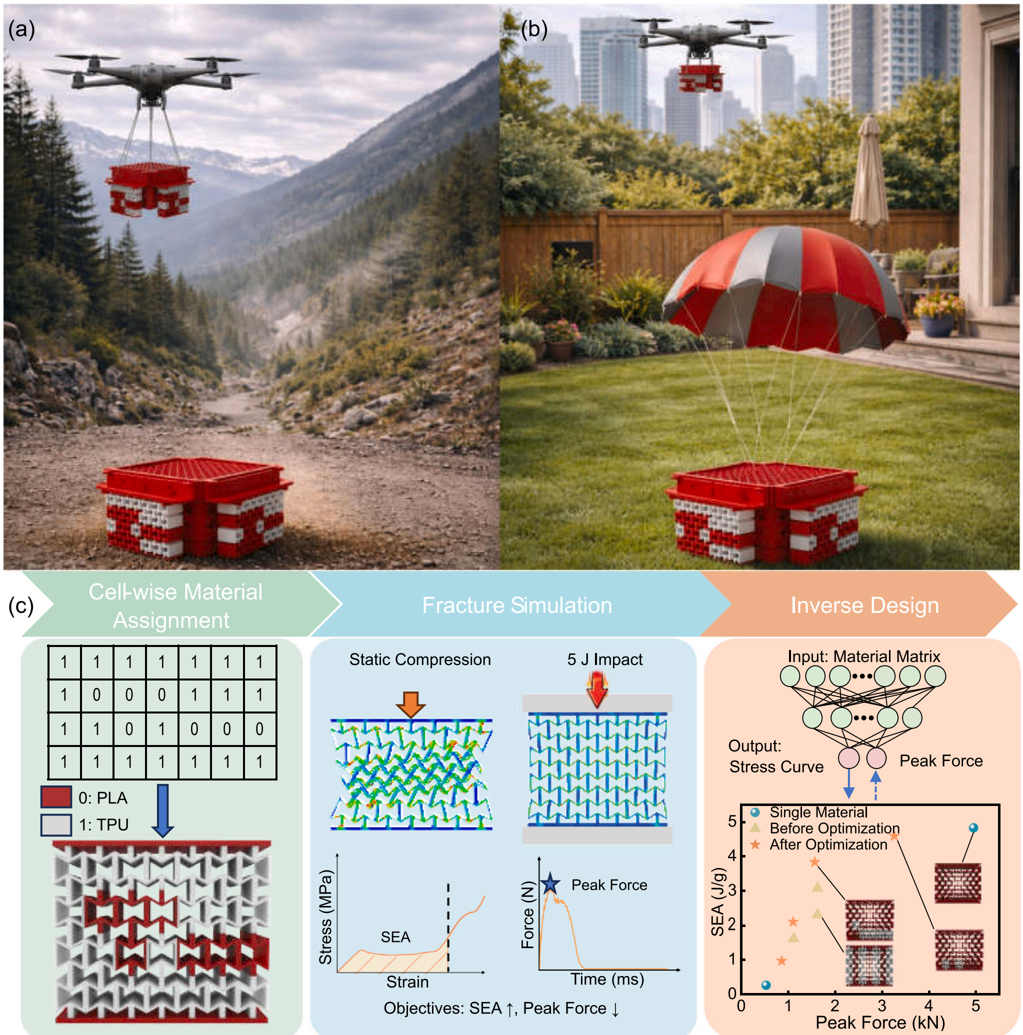

Fig. 1. Application scenarios and inverse design framework for heterogeneous multi-material energy-absorbing metamaterials. (a) Drone-based delivery in remote areas, where packages are subjected to direct ground impact. (b) Last-mile delivery scenario with additional buffering mechanisms (e.g., parachute-assisted landing). (c) Overall design workflow: cell-wise material assignment is defined by a binary material matrix (PLA/TPU), followed by fracture-aware finite element simulations under static compression and impact loading to obtain stress–strain response and peak force. A machine-learning-based inverse design model is then established to map material layouts to mechanical responses, enabling efficient multi-objective optimization. The design objective is to simultaneously maximize specific energy absorption (SEA) and minimize peak force.

directly into the inverse-design basis through fracture-aware finite-element simulations under quasi-static compression and dynamic impact. A dual-response Transformer surrogate is trained to predict the complete nominal stress–strain response and peak impact force and is subsequently coupled with NSGA-II to explore the large combinatorial material-layout space. Third, a structural-scale topology–mechanics framework is established for heterogeneous multi-cell material organization. Composition-controlled analysis of the complete Pareto population shows that connected TPU paths promote compliant and progressive deformation to suppress peak force, whereas continuous PLA networks form load-bearing skeletons that increase the sustained crushing load and SEA. These results establish a direct relationship between non-periodic multi-cell material organization, structural load paths, and the SEA–peak-force trade-off.

The remainder of the paper is organized as follows. Section 2 presents the geometry and material-layout representation, constitutive and fracture models, finite-element implementation, dataset construction, surrogate model, multi-objective optimization, specimen fabrication, and experimental procedures. Section 3 reports the validation of the constitutive framework and surrogate model, the Pareto-optimal material layouts and their deformation mechanisms, and the UAV airdrop performance. Section 4 summarizes the principal findings and discusses the limitations and future development of the proposed framework. Additional model definitions, parameter studies, and validation results are provided in the Supporting Information.

2. Materials and methods

This section describes the procedures used to construct and evaluate the inverse-design framework summarized in Fig. 1. The geometry and material-layout representation are first defined, followed by the constitutive and fracture models, finite-element implementation, dataset construction, Transformer-based surrogate model, multi-objective optimization procedure, specimen fabrication, and mechanical testing. Standard constitutive equations and supplementary sensitivity analyses are provided in the Supporting Information to maintain the continuity of the main text.

For clarity, the inverse-design problem can be written in terms of a binary design vector $\mathbf{x} = (x_1, \ldots, x_{28}) \in \{0,1\}^{28}$, where $x_i = 0$ denotes PLA and $x_i = 1$ denotes TPU in the ith cell. The fracture-aware finite-element operator maps $\mathbf{x}$ to the nominal stress–strain response $\boldsymbol{\sigma}(\mathbf{x})$

and the impact-force history $\mathbf{F}(\mathbf{x})$. The trained surrogate $\widehat{\mathcal{M}}_\theta$ approximates this operator and provides the derived objectives $\widehat{\mathrm{SEA}}(\mathbf{x})$ and $\widehat{F}_{\mathrm{peak}}(\mathbf{x})$. The multi-objective search therefore seeks the non-dominated set associated with $\min_{\mathbf{x}\in\{0,1\}^{28}}[-\widehat{\mathrm{SEA}}(\mathbf{x}), \widehat{F}_{\mathrm{peak}}(\mathbf{x})]$, subject to the fixed lattice geometry, constituent-material properties, loading conditions, and fabrication constraints defined below. This formulation isolates material organization as the design variable while keeping the lattice geometry, constituent materials, loading conditions, and fabrication constraints fixed.

2.1. Geometry and material layout representation

The investigated metamaterial was constructed from a two-dimensional re-entrant hexagonal lattice. The structure consisted of a 4×7 array of unit cells, corresponding to four rows and seven columns. The lattice geometry was kept fixed throughout the study, while the design freedom was introduced through cell-wise material assignment. Each design was encoded as a binary material-layout matrix, where 0 denotes PLA and 1 denotes TPU. The entries of the matrix were ordered from left to right and from top to bottom. In the finite-element model, the 28 unit cells in the designable lattice region were assigned according to this binary matrix, whereas the upper and lower supporting plates were not included in the design variables and were fixed as PLA. The unit-cell geometry and dimensional parameters are provided in Section S1 of the Supporting Information.

2.2. Constitutive and fracture modeling

To establish a physically consistent basis for dataset generation and subsequent optimization, different constitutive descriptions were adopted for the two constituent materials. TPU was represented using an Ogden hyperelastic model, whereas the pre-damage response of PLA was described using a rate-independent Johnson–Cook hardening model. The corresponding constitutive equations and material parameters are provided in Section S2 of the Supporting Information. Because the Johnson–Cook hardening relation alone cannot represent the experimentally observed post-peak degradation of PLA, the following ductile damage formulation was incorporated into the PLA model.

The degradation of the PLA phase was described using a ductile damage formulation [92] comprising damage initiation and subsequent damage evolution. Damage initiation was described by an equivalent-plastic-strain-based ductile criterion,

$$\omega_D = \int \frac{d\bar{\varepsilon}^{pl}}{\bar{\varepsilon}_f^{pl}(\eta, \dot{\bar{\varepsilon}}^{pl})} = 1, \tag{1}$$

where ω_D is the damage accumulation variable, and $\bar{\varepsilon}_f^{pl}(\eta, \dot{\bar{\varepsilon}}^{pl})$ denotes the equivalent plastic strain at damage initiation as a function of stress triaxiality η and equivalent plastic strain rate $\dot{\bar{\varepsilon}}^{pl}$. This criterion provides a direct mechanistic interpretation of the onset of local failure: regions where plastic strain accumulates fastest under the given stress state will first satisfy $\omega_D = 1$ and enter the damage stage. For the PLA lattice considered here, the inclined struts and node joints near the loading end experience pronounced bending and geometric constraint and are therefore expected to reach the damage-initiation condition before the less constrained regions.

After damage initiation, a displacement-based evolution law was adopted,

$$\bar{u}^{pl} = L\,\bar{\varepsilon}^{pl}, \tag{2}$$

$$D = \frac{\bar{u}^{pl}}{\bar{u}_f^{pl}}, \qquad 0 \le D \le 1, \tag{3}$$

where L is the characteristic element length and $\bar{u}_f^{pl}$ is the equivalent plastic displacement at complete failure. With increasing D, the local stiffness and load-carrying capacity degrade progressively until final failure is reached. This evolution law is directly linked to the macroscopic response of the lattice: once the most highly stressed PLA members begin to soften, the original load-transfer path is weakened, adjacent members are forced to carry more load, and the structural response shifts from continued hardening to load degradation or reduced plateau stress. In other words, the role of the damage evolution model is to convert local member failures into global load drops, peak-force reductions, and changes in SEA due to stiffness loss and load redistribution. The influence of the ductile damage formulation on the pure-PLA structural response is assessed in Section 3.1.

2.3. Finite element simulations

This subsection describes the dimensional idealization, element formulation, constitutive implementation, contact interactions, boundary conditions, loading conditions, and response extraction used in the quasi-static and dynamic finite-element analyses. The assumptions associated with the plane-strain formulation and effective material descriptions are also stated, together with the corresponding sensitivity analyses. Finite-element simulations were performed in Abaqus/Explicit using a two-dimensional plane-strain formulation with an assigned section thickness of 20 mm. The plane-strain approximation was adopted because the lattice geometry, cell-wise material assignment, and nominal loading conditions were approximately uniform through the specimen thickness, while the primary quantities of interest were the in-plane crushing response, SEA, and transmitted peak force. This formulation also enabled consistent generation of the large finite-element dataset required for surrogate-model training and optimization. However, it suppresses out-of-plane strain and therefore does not explicitly resolve free-surface effects, through-thickness variations, or three-dimensional instability and fracture modes. CPE4R plane-strain elements with reduced integration were selected as the primary element formulation. Although CPE3 was included in the element-type assignment as a fallback option for automatic meshing, the generated specimen meshes consisted entirely of CPE4R elements, and no CPE3 elements were present in the meshes used in the sensitivity study. General contact was defined using hard normal contact with separation allowed and penalty-based tangential behavior with a friction coefficient of 0.2.

TPU was modeled using a fourth-order Ogden hyperelastic model, whose parameters were fitted in Abaqus using the tensile responses of printed dog-bone specimens. PLA was modeled using linear elasticity, Johnson–Cook plasticity, and ductile damage with element deletion. The PLA Young's modulus and the Johnson–Cook initial yield parameter A were determined from tensile tests of printed dog-bone specimens, whereas the density and Poisson's ratio were obtained from the material manufacturer. Because the available tensile tests did not provide sufficient post-yield and fracture information for independently identifying the Johnson–Cook hardening parameters B and n and the ductile-damage parameters, these parameters were obtained through iterative inverse identification using the compression response of the pure PLA lattice. The sources of the material parameters and the complete inverse-identification procedure are detailed in Section S2 of the Supporting Information.

PLA and TPU were treated as homogeneous and isotropic effective continua. Because the constitutive parameters were identified using specimens fabricated under the same printing conditions as the structural samples, the calibrated responses partially incorporate the aggregate influence of the investigated manufacturing process. Nevertheless, individual filament paths, interlayer anisotropy, internal voids, residual stresses, local geometric deviations, and specimen-to-specimen variability were not explicitly represented. The identified parameters should therefore be regarded as effective parameters applicable to the investigated printing conditions, structural scale, and loading range rather than as universally transferable intrinsic material constants.

The strain-rate and thermal-softening terms of the Johnson–Cook model were set to zero because independent rate-dependent and temperature-dependent material data were not available for parameter identification. The experimental comparison at the investigated impact-energy level supports the use of the effective model under the present loading conditions, but its applicability to substantially different impact velocities or temperatures was not evaluated. The TPU–PLA interfaces were represented by shared nodes, corresponding to a perfect-bonding assumption without explicit interfacial sliding, debonding, or cohesive failure. Consequently, the numerical model describes the global response of the structures under the investigated fabrication conditions but does not separately quantify the effects of arbitrary interface defects or weak interfacial bonding. These assumptions provide a consistent basis for comparing different material layouts within the investigated design and fabrication space. When extending the model to substantially different specimen thicknesses, printing qualities, interface strengths, impact velocities, or temperature conditions, the associated three-dimensional and manufacturing effects may require additional consideration.

For quasi-static compression simulations, the lower boundary of the specimen was fully fixed, and a vertical displacement of 30 mm was applied to the upper reference point. Since the initial specimen height was 60 mm, the maximum nominal compressive strain was 0.5. The displacement was applied using a linear tabular amplitude. The vertical displacement and reaction force at the loading reference point were recorded to obtain the load–displacement response used for structural-level comparison in Figs. 2 and 5. The same force and displacement data were converted to nominal stress and nominal strain only for consistent response sampling and SEA calculation across different layouts; these normalized quantities were not interpreted as intrinsic continuum material properties. The corresponding mesh-sensitivity and quasi-static energy-verification results are provided in Section S3.

For dynamic impact simulations, a rigid impactor with a mass of 2.5 kg was assigned an initial downward velocity of 2000 mm/s, corresponding to an impact energy of 5 J. Gravity was included with an acceleration of 9810 mm/s^2. The lower support was fully fixed. The transmitted force was obtained from the vertical reaction force of the fixed bottom support, and the peak force was defined as the maximum value of the force–time history. The dynamic step time was 0.025 s with 400 output intervals. The characteristic lattice mesh size was 0.75 mm, and the impactor/support parts were seeded with a 0.6 mm mesh. All dynamic simulations and peak-force data used for surrogate-model training and optimization were generated under the same prescribed impact condition, with an impact energy of 5 J and an initial velocity of 2000 mm/s. The corresponding impact experiments were conducted under the same loading condition. Mesh sensitivity was evaluated using four representative material layouts and four characteristic specimen mesh sizes of 1.00, 0.75, 0.60, and 0.50 mm under both quasi-static compression and dynamic impact. For every quasi-static case, SEA was evaluated using the common strain interval from 0 to 0.3 and the layout-dependent mass normalization defined above. Taking the 0.50 mm mesh as the reference, the 0.75 mm production mesh resulted in SEA differences of 0.81%–3.78% and peak-impact-force differences of 1.68%–6.07% across the four layouts. These differences were below the adopted 10% engineering tolerance. Complete numerical comparisons and convergence results are provided in Section S3.

2.4. Dataset construction and performance metrics

This subsection describes the sampling of the binary material-layout space, the division of the finite-element data into training, validation, and test subsets, and the processing of the quasi-static and dynamic responses. The calculation of SEA, response normalization, dataset-coverage assessment, and construction of the extrapolation challenge are also specified. A finite-element dataset was constructed from 8000 unique binary material-layout matrices. In the matrix encoding, 0 and 1 represent PLA and TPU, respectively. Letting k denote the number of TPU cells, a layout at a prescribed material ratio was generated by randomly shuffling a list containing k ones and $28 - k$ zeros and reshaping it into a 4×7 matrix; exact duplicate matrices were rejected. Because only integer cell counts are admissible, the realized TPU fraction is $k/28$. The sampling was stratified by material count: the intermediate strata $k = 3, \ldots, 25$ contained 337–344 layouts each, whereas the corner strata were intentionally sparse. The resulting dataset contained 169 near-corner or corner layouts with $k \leq 2$ or $k \geq 26$, including one all-PLA and one all-TPU layout. This design provides broad coverage across intermediate material ratios without implying exhaustive coverage of the complete 2^{28} combinatorial space. For every layout, quasi-static compression simulations were used to obtain the nominal stress–strain curve, and dynamic impact simulations were used to extract the peak impact force.

The stress–strain curve was sampled from 0 to 0.5 strain using 201 uniformly spaced points. The dataset was divided by model index into 4000 training samples, 2000 validation samples, and 2000 test samples. All 8000 matrices were checked to be unique, so no exact layout occurred in more than one subset. Input-space composition, morphology, nearest-training-layout distance, and output-response distributions were compared separately among the three subsets, as detailed in Section S4 and Figure S3 of the Supporting Information. The stress values were reported in MPa, peak force in N, and SEA in J/g.

The homogeneity of the three subsets was evaluated using the TPU-cell-count distribution, cell-wise TPU occurrence frequency, heterogeneous-material interfaces, connected-region descriptors, and principal-component analysis of the standardized morphology descriptors. SEA, peak-force, and curve-response distributions were also compared. In addition, the minimum Hamming distance from each validation and test layout to the training set was calculated to distinguish in-distribution interpolation from extrapolation in material-layout space.

SEA was calculated from the absorbed work per unit mass as $\mathrm{SEA} = m^{-1} \int_0^{u_{0.3}} F(u)\,\mathrm{d}u = (V/m) \int_0^{0.3} \sigma_{\mathrm{nom}}(\varepsilon_{\mathrm{nom}})\,\mathrm{d}\varepsilon_{\mathrm{nom}}$, where F and u are the structural load and displacement, respectively, $u_{0.3}$ is the displacement corresponding to a nominal compressive strain of 0.3, V is the nominal specimen volume, and m is the layout-dependent specimen mass. The mass was determined from the numbers of PLA and TPU cells in each layout using densities of 1.21 and 1.20 g/cm^3, respectively. Thus, although the complete stress–strain response was sampled up to a strain of 0.5, only the response between strains 0 and 0.3 was included in the SEA calculation [93]. The same integration limit and mass-normalization procedure were used for dataset construction, surrogate-model evaluation, inverse optimization, mesh-sensitivity analysis, and damage-parameter sensitivity analysis. The stress curves were normalized pointwise using the training-set mean and standard deviation at each sampled strain coordinate, whereas peak force was normalized using the scalar mean and standard deviation calculated from the training set. The same normalization parameters were used for validation, testing, and inverse optimization.

2.5. Transformer-based surrogate model

To enable rapid evaluation of the mechanical response over this dataset, a Transformer-based surrogate model [94] was developed for the joint prediction of the stress–strain curve and peak force, as shown in Fig. 3a. The 4×7 binary material-layout matrix was first flattened into a sequence of 28 tokens, and each token was embedded together with its 2D positional information to preserve the spatial arrangement of the material distribution. The embedded sequence was then processed by stacked Transformer encoder blocks to capture the long-range interactions among different unit cells induced by the non-periodic TPU/PLA assignment. After global pooling, the encoded features were mapped to a latent representation z, which served as the shared structural descriptor for the subsequent dual-response prediction. In the

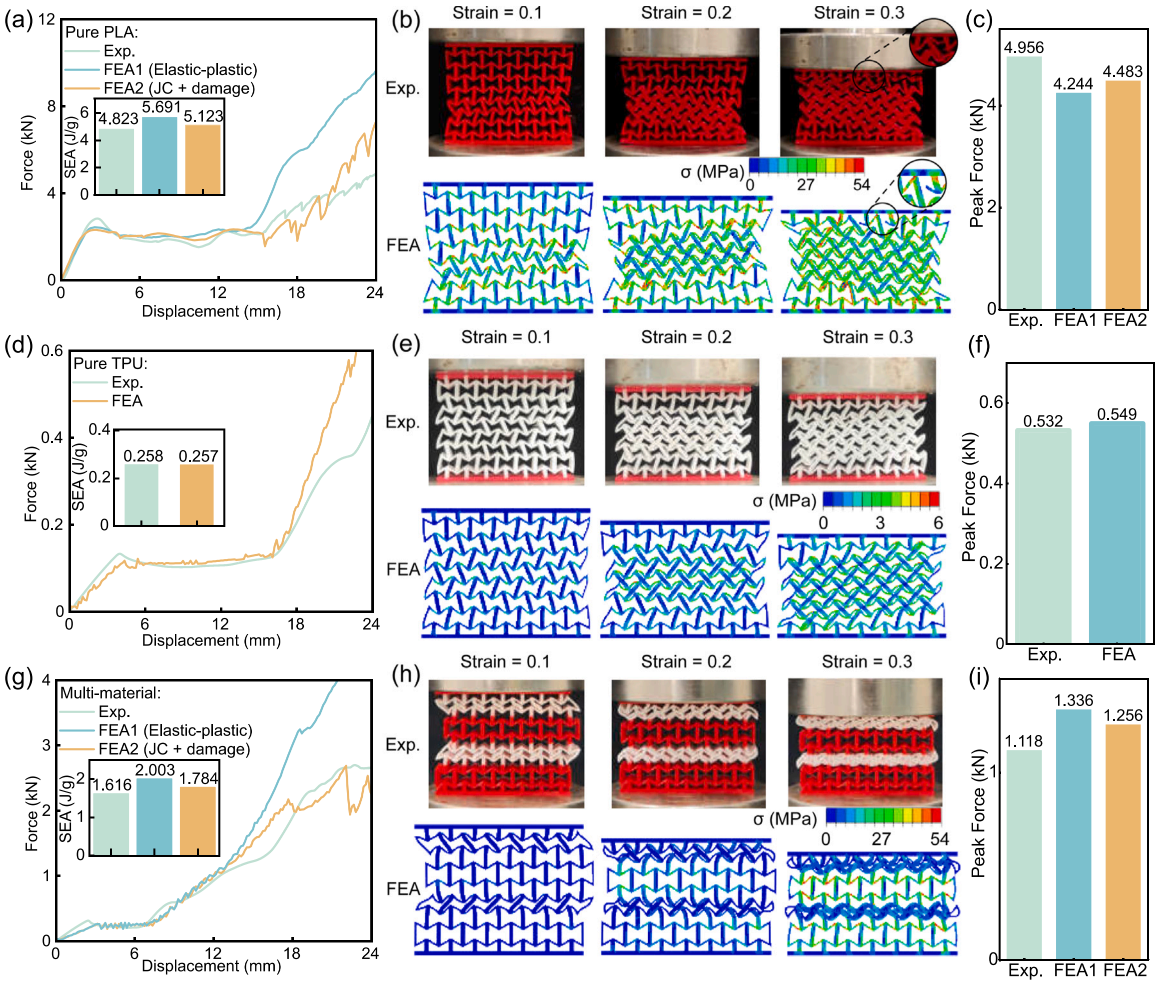

Fig. 2. Experimental and numerical validation of different material systems. (a–c) Pure PLA structures: (a) load–displacement response with comparison between experiments and finite-element analysis (FEA); (b) Deformation modes at selected nominal compressive strains; (c) Peak force comparison. (d–f) Pure TPU structures: corresponding load–displacement response, deformation evolution, and peak force results. (g–i) Multi-material structures: combined mechanical response and deformation patterns, highlighting the interaction between soft and hard phases. The pure PLA compression response was used for structural-level parameter identification, whereas the remaining cases were used for subsequent structural-level assessment. The agreement supports the adequacy of the effective constitutive framework under the investigated printing and loading conditions.

peak-force branch, the latent feature was directly mapped to the peak force under the 5 J impact condition. In the curve branch, the stress response was generated in a strain-conditioned manner,

$$\sigma(\varepsilon_k) = f(z, \varepsilon_k) \tag{4}$$

where ε_k denotes the kth sampled strain coordinate and $k = 1, 2, \ldots, N$. In the present study, the strain range from 0 to 0.5 was uniformly discretized into $N = 201$ points. Rather than predicting the complete curve as a monolithic fixed-length output vector, the decoder was evaluated at all prescribed strain coordinates, and the full stress–strain curve was reconstructed by collecting the corresponding stress predictions. This formulation represents the stress response as a strain-conditioned function of the latent structural descriptor.

To align the learning objective with the engineering targets, a joint loss function was adopted for the simultaneous optimization of the stress–strain curve and impact peak force,

$$\mathcal{L} = \lambda_c \mathcal{L}_{\mathrm{curve}} + \lambda_f \mathcal{L}_{\mathrm{force}} \tag{5}$$

where $\mathcal{L}_{\mathrm{curve}}$ and $\mathcal{L}_{\mathrm{force}}$ denote the loss terms for the stress–strain curve and the impact peak force, respectively, while λ_c and λ_f are the corresponding weighting coefficients. Although SEA is obtained by integrating the entire stress–strain curve, the low-strain response contains the initial stiffness and collapse-onset characteristics that govern the transition into the subsequent energy-absorbing regime. Prediction errors in this stage may shift the onset of progressive collapse and consequently affect the reconstructed response over a substantially wider strain range. The curve loss was therefore formulated in a strain-weighted form,

$$\mathcal{L}_{\mathrm{curve}} = \frac{1}{N}\sum_{k=1}^{N} w(\varepsilon_k)\,\ell\big(\hat{\sigma}(\varepsilon_k),\, \sigma(\varepsilon_k)\big) + \lambda_{y0}\mathcal{L}_{y0}, \tag{6}$$

where N is the number of sampled strain points, ε_k is the kth sampled strain coordinate, and $\hat{\sigma}(\varepsilon_k)$ and $\sigma(\varepsilon_k)$ denote the predicted and finite-element reference stresses at ε_k, respectively. The function $w(\varepsilon_k)$ is the strain-dependent weighting function, while $\ell(\hat{\sigma}(\varepsilon_k), \sigma(\varepsilon_k))$ denotes the pointwise Huber loss. The term $\mathcal{L}_{y0}$ constrains the initial point of the predicted curve, and λ_{y0} controls its relative contribution to the curve loss. The weighting function and its selected values are specified in the following equation, whereas the Huber-loss definition, evaluation metrics, and hyperparameter-sensitivity results are provided in Section S6 of the Supporting Information. The surrogate model was implemented in TensorFlow/Keras. In the specific implementation, the 28 material tokens obtained from the $4 \times 7 \times 1$ binary layout were embedded into a 64-dimensional feature space. Two-dimensional positional embedding was added to retain the spatial information of the unit-cell arrangement. The token sequence was then processed by three

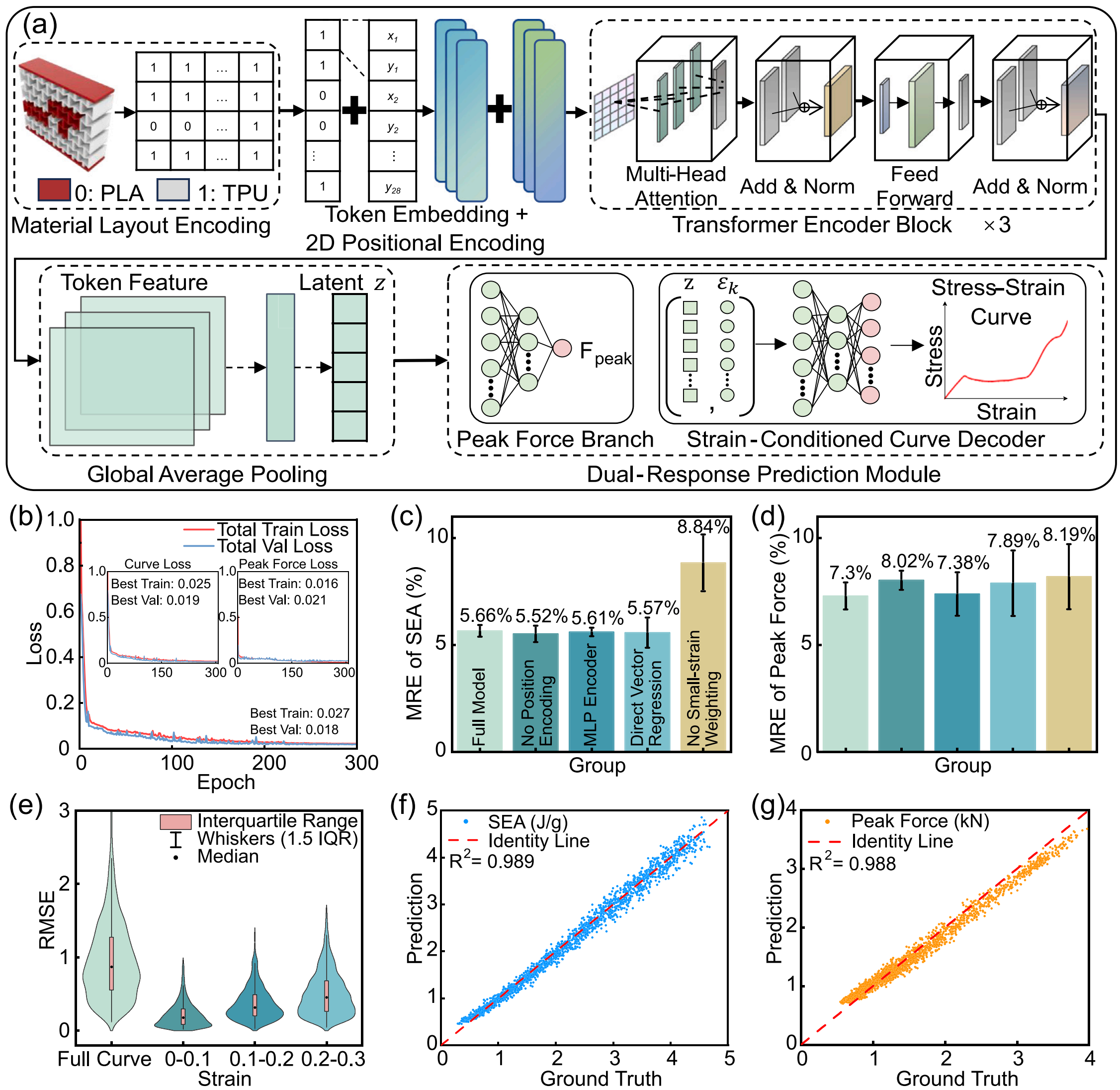

Fig. 3. Transformer-based dual-response prediction framework for heterogeneous multi-material metamaterials. (a) Network architecture, where the binary material layout is first encoded into token features with 2D positional embedding and processed by stacked Transformer encoder blocks; a dual-branch decoder is then employed to simultaneously predict the full nominal stress–strain curve and the peak force. (b) Training and validation loss curves, showing stable convergence of both curve and force predictions. (c,d) Ablation studies quantifying the contributions of positional encoding, encoder structure, and loss design to prediction accuracy in terms of mean relative error (MRE) for SEA and peak force. The reported bar values represent the mean over five random seeds, and the error bars denote the corresponding standard deviation. (e) Root mean square error (RMSE) distribution across different strain intervals, highlighting improved accuracy in the small-strain regime. (f,g) Comparison between predicted and ground-truth values for SEA and peak force, demonstrating high prediction fidelity and strong generalization capability.

Transformer encoder blocks with four attention heads and a dropout rate of 0.2. The encoded features were aggregated by global average pooling and mapped to a 128-dimensional latent representation.

The latent representation was shared by two output branches. The curve branch used a strain-conditioned decoder to generate the 201-point stress–strain response over the strain range of 0 to 0.5. Specifically, the latent representation was concatenated with each prescribed strain coordinate and passed through two fully connected layers with 256 hidden units and GELU activation to predict the stress at each strain point. The force branch consisted of fully connected layers with 128 and 64 hidden units and GELU activation, followed by a linear output layer for peak-force prediction.

The model was trained using the joint loss function defined in Eqs. (5) and (6). The loss weights for the curve and force branches were set to $\lambda_c = 0.8$ and $\lambda_f = 0.2$, respectively. The force loss was defined as the mean squared error. The curve loss was implemented as a small-strain-weighted Huber loss with an additional initial-point constraint.

The strain-dependent weight in Eq. (6) was defined as

$$w(\varepsilon_k) = \begin{cases} w_{\mathrm{hi}}, & \varepsilon_k \le \varepsilon_{\mathrm{focus}}, \\ w_{\mathrm{lo}}, & \varepsilon_k > \varepsilon_{\mathrm{focus}}, \end{cases} \tag{7}$$

where $\varepsilon_{\mathrm{focus}}$ controls the strain range receiving additional emphasis. In the final model, $\varepsilon_{\mathrm{focus}} = 0.16$, $w_{\mathrm{hi}} = 12.0$, and $w_{\mathrm{lo}} = 1.0$.

The model was trained using the Adam optimizer with an initial learning rate of 10^{-3}. The batch size was 128, and the maximum number of epochs was 600. Early stopping was applied with a patience of 50 epochs based on validation loss, and the learning rate was reduced by a factor of 0.5 if the validation loss did not improve for 20 epochs. The model with the lowest validation loss was saved and used for subsequent inverse optimization.

Training-set-size sensitivity was evaluated using nested, TPU-count-stratified subsets containing 500, 1000, 2000, 3000, and 4000 training samples. Five random seeds (11, 22, 33, 44, and 55) were used at each size, while the original validation and test sets remained fixed. All normalization statistics were recalculated from the corresponding training subset. A performance plateau was declared only when the 3000-to-4000 relative improvement was below 5% and the absolute mean change was smaller than the pooled across-seed standard deviation for SEA MRE, peak-force MRE, and full-curve RMSE.

A material-composition extrapolation challenge was constructed from all 169 layouts satisfying $k \leq 2$ or $k \geq 26$. These layouts were removed from both the training and early-stopping validation sets, and the remaining layouts with $3 \leq k \leq 25$ were used for model fitting. The challenge results were reported separately from the conventional test results because they evaluate extrapolation in material ratio rather than interpolation within the random-split distribution.

To assess whether the prediction accuracy depended specifically on the Transformer encoder, parameter-matched multilayer perceptron (MLP), convolutional neural network (CNN), and graph convolutional network (GCN) alternatives were trained using the same five seeds. All encoders mapped the 4×7 layout to a 128-dimensional latent representation and shared the same curve head, peak-force head, data partitions, training-set-based normalization, loss functions, and optimization protocol. The MLP used three 256-unit hidden layers. The CNN used four 3×3 convolutional layers with 64, 64, 64, and 128 filters, ReLU activation, layer normalization, and no dropout in the convolutional encoder. The GCN used the fixed horizontal–vertical grid adjacency with self-loops and four 192-dimensional graph-convolution layers. The parameter counts of the alternative models were constrained to within $\pm 15\%$ of the Transformer parameter count.

2.6. Multi-objective optimization and clustering

The trained surrogate model was coupled with NSGA-II [95,96] for multi-objective inverse design. Each individual was represented as a 28-bit binary vector and reshaped into a 4×7 material-layout matrix during evaluation. The two optimization objectives were to minimize the peak force and maximize SEA. For each candidate design, the surrogate model predicted the normalized stress curve and peak force, which were then denormalized before calculating the objective values.

The NSGA-II algorithm was implemented using DEAP. Unless otherwise stated, the final inverse-design optimization was performed with a population size of 1000 and a maximum of 120 generations. Offspring were generated from the current population using DEAP's variation operators, and the next generation was selected from the combined parent–offspring population using the NSGA-II non-dominated sorting and crowding-distance procedure implemented in `tools.selNSGA2`. Uniform crossover and bit-flip mutation were used as the genetic operators. Following the DEAP parameter naming convention, `cxpb` denotes the probability that an offspring pair undergoes crossover, `mutpb` denotes the probability that an offspring individual undergoes mutation, and `indpb` denotes the independent bit-level mutation probability in the bit-flip mutation operator. The final settings were `cxpb` = 0.7, `mutpb` = 0.2, and `indpb` = 0.1. For uniform crossover, the per-bit exchange probability was fixed at 0.5. Convergence was monitored using the hypervolume of the current non-dominated Pareto front, and the optimization was stopped when the hypervolume did not improve for 15 consecutive generations or when the maximum generation number was reached. Duplicate material matrices were removed during post-processing.

The robustness of the NSGA-II settings was examined through one-factor-at-a-time variations of the population size, crossover probability, individual-level mutation probability, and bit-level mutation probability. The hypervolume definition, reference-point selection, sensitivity protocol, and convergence results are provided in Section S7 of the Supporting Information.

2.7. Fabrication and mechanical testing

This subsection describes the fabrication of the multi-material specimens and the laboratory procedures used for structural-level validation. Dual-nozzle fused deposition modeling (FDM) was used for specimen preparation, followed by quasi-static compression and drop-weight impact tests conducted under loading conditions corresponding to those adopted in the finite-element analyses. All specimens were fabricated using dual-nozzle fused deposition modeling with a Raise3D E2 printer. PLA and TPU 95A filaments purchased from Raise3D were used as the hard and soft phases, respectively. The extrusion line width was 0.4 mm, and the layer height was 0.2 mm. The nozzle temperature was 220 °C, the bed temperature was 60 °C, and the default printing speed was 60 mm/s. No post-processing was applied after printing.

Quasi-static compression tests were conducted using a CMT6104 universal testing machine equipped with a 10 kN load cell. The specimens were compressed at a displacement rate of 2 mm/min until a nominal compressive strain of 0.5 was reached. Each test was repeated three times, and the averaged response was used for comparison with the simulations. The quasi-static compression tests followed a monotonic loading protocol and were terminated after the prescribed maximum displacement was reached. A controlled unloading stage was not included; therefore, unloading paths and residual displacements were not recorded in the present experiments.

Drop-weight impact tests were conducted using a 2.5 kg mass released from a height of 20 cm, corresponding to an impact energy of approximately 5 J. The transmitted impact force was measured using an NOS F306 force sensor at a sampling frequency of 2000 Hz. The peak force was defined as the maximum value over the entire force–time history. Each impact test was repeated three times, and the averaged peak force was reported.

2.8. UAV airdrop experiments

Application-level airdrop tests were conducted using an SG909 UAV. Protective boxes fabricated with pure PLA, pure TPU, and the optimized multi-material layout were tested. For the landing-snapshot comparison shown in Fig. 6a–c, the boxes were released from a height of 1.5 m. For payload-protection tests, the drop height was increased to 2 m for all three designs. Each box had a mass of 372 g. Two raw eggs were placed inside the box as fragile payloads, and the total mass of the box and payload was approximately 490 g.

A WT901WIFI acceleration sensor was fixed inside the box to record the acceleration response during landing. The sampling frequency was 200 Hz. Each design was tested three times. The protection was considered successful when both eggs remained intact after landing, with no visible cracks or breakage. The landing process and the post-impact payload state were recorded for comparison among the pure PLA, pure TPU, and optimized multi-material boxes.

3. Results and discussion

Based on the modeling, dataset-generation, surrogate-training, optimization, and experimental procedures described above, this section presents the structural-level validation of the constitutive framework, the predictive performance and generalization capability of the surrogate model, the resulting Pareto-optimal material layouts, and their underlying deformation mechanisms and application-level performance.

3.1. Constitutive and fracture model validation

The effective constitutive framework was examined using pure-PLA, pure-TPU, and multi-material lattices under quasi-static compression and impact loading. Fig. 2 compares the numerical and experimental load–displacement responses, deformation modes, and peak impact forces for the three material systems.

As shown in Fig. 2a–c, the elastic–plastic PLA model preserves excessive load-carrying capacity after yielding and consequently overestimates the post-yield load, SEA, and impact peak force. Incorporating ductile damage enables progressive stiffness degradation and produces closer agreement with the experimental load–displacement response, failure morphology, and peak force. For the pure-TPU lattice, Fig. 2d–f shows that the Ogden formulation reproduces the nonlinear load–displacement response, large-deformation morphology, and impact peak force with good agreement.

For the multi-material lattice, the dominant load-bearing skeleton is still mainly provided by the PLA phase, and stress concentration is therefore expected to remain highest in the PLA struts located along the principal compressive load path, particularly near the loading end and in regions adjacent to the TPU phase where deformation incompatibility enhances local bending. Unlike the pure PLA lattice, however, the presence of TPU allows part of the deformation to be accommodated by the soft phase, thereby mitigating crack propagation and delaying the formation of macroscopically visible fracture. Consequently, the primary effect of damage in the multi-material structure is not necessarily the appearance of obviously broken members within the observed strain range, but rather the progressive degradation of local PLA stiffness and the rerouting of internal load transfer. This is why the elastic–plastic model still overestimates the post-yield load level, SEA, and impact peak force even when no pronounced macroscopic fracture is observed in Fig. 2h, whereas much better agreement is achieved once progressive damage is included, as shown in Fig. 2g–i.

Overall, these results indicate that the Ogden model is sufficient for the TPU phase, whereas progressive damage modeling is essential for lattices containing PLA, thereby providing a physically reliable basis for the subsequent dataset construction and surrogate-assisted optimization. The robustness of the calibrated damage formulation was further evaluated using a representative near-balanced multi-material layout containing 13 PLA cells and 15 TPU cells. With a specimen mesh size of 0.60 mm, the damage-initiation strain and failure displacement were independently perturbed by $\pm 20\%$. Relative to the baseline SEA of 1.820 J/g, calculated over the strain interval from 0 to 0.3, the perturbed cases produced SEA values of 1.813–1.917 J/g, corresponding to changes from −0.38% to +5.33%. The dynamic peak-force changes remained between −0.55% and +0.63%. These results show that the predicted global responses are reasonably robust to moderate perturbations of the calibrated damage parameters within the investigated range. The selected layout and detailed sensitivity results are provided in Section S3.

3.2. Surrogate-model performance and generalization

Following the dataset-construction and training procedures described in the Methods section, the predictive performance of the surrogate model was evaluated using the independent test set. Fig. 3 summarizes the model architecture, training convergence, ablation results, strain-dependent curve errors, and agreement between the surrogate predictions and finite-element reference values. The dataset-coverage, training-size, and material-composition extrapolation analyses were further used to define the scope of the resulting generalization claims.

As shown in Fig. 3b, the total, curve, and peak-force losses decreased rapidly during the initial training stage and subsequently approached stable plateaus. The training and validation histories remained close throughout the optimization, with no pronounced generalization gap, indicating stable convergence without evident overfitting under the selected training protocol. The ablation results in Fig. 3c,d further quantify the influence of the individual model components. For SEA prediction, removing the small-strain weighting produced the largest increase in error among the tested variants. This pronounced deterioration can be interpreted from the progressive deformation sequence of the lattice. The additionally weighted interval, $\epsilon \leq 0.16$, encompasses the initial bending and rotation of the cell walls, the establishment of the principal load-transfer paths, and the onset of the first local collapse events. For the aperiodic TPU/PLA layouts considered here, these early-stage responses are sensitive to the local soft–hard stiffness contrast and the connectivity of the relatively stiff load-bearing regions, which influence where and when progressive collapse is initiated. Without the strain-dependent weighting, the broader intermediate- and high-strain portions contain a larger number of sampled points and therefore contribute more strongly to the aggregate pointwise curve loss. The network may consequently obtain a relatively low averaged loss while retaining noticeable errors in the initial stiffness, first load maximum, or collapse-onset strain. Such errors are not necessarily confined to the weighted interval: an inaccurate prediction of the first instability can shift the transition into the subsequent plateau regime and introduce a persistent stress or strain offset over a wider portion of the reconstructed curve. Since SEA is calculated from the integral of this full response, these deviations accumulate into a substantial area error. The small-strain weighting therefore acts as a physics-guided constraint that encourages the shared latent representation to retain material-layout features associated with collapse initiation and load-path evolution. These features also influence the subsequent progressive-collapse and plateau responses, explaining why removal of the weighting term markedly degrades the curve-derived SEA prediction. Importantly, this result does not imply that the low-strain interval directly contributes the largest proportion of SEA; rather, this interval contains the deformation-trigger information governing entry into the principal energy-absorbing regime. Other ablation variants, including removing positional encoding, replacing the Transformer encoder with a multilayer perceptron (MLP), and replacing the strain-conditioned curve decoder with a direct fully connected output layer, result in smaller performance degradation. This indicates that, although spatial encoding, global-interaction modeling, and strain-conditioned decoding all contribute to the model performance, the strain-aware loss design plays the most critical role in improving the curve-related objective. For peak-force prediction in Fig. 3d, all tested variants show relatively limited error variation compared with the SEA task, suggesting that the force branch is less sensitive to the examined curve-modeling components and that the shared latent representation remains robust for impact-force prediction. Overall, these results indicate that the proposed architecture provides stable dual-response prediction, while the small-strain-weighted loss plays the dominant role in improving SEA-related curve prediction.

The local fitting characteristics of the reconstructed curves were further analyzed in Fig. 3e. The full-curve RMSE exhibited the broadest distribution, whereas the $\epsilon \in [0, 0.1]$ interval showed the smallest and most concentrated RMSE values. This reduced error is consistent with the additional emphasis assigned to the low-strain response during training. In comparison, the $[0.1, 0.2]$ and $[0.2, 0.3]$ intervals exhibited larger and more dispersed errors. Physically, these intermediate strain ranges correspond to the transition from initial cell-wall bending and rotation to progressive collapse. During this stage, local PLA damage initiation and stiffness degradation may interact with the large rotation and deformation of the TPU regions, while evolving cell contact and load-path redistribution introduce additional layout-dependent nonlinearities. These mechanisms can produce rapid changes in tangent stiffness, localized stress drops, and shifts in collapse sequence, resulting in a less smooth and more sample-dependent stress–strain response than that observed in the initial deformation regime. The increased intermediate-strain RMSE should therefore be interpreted as a consequence of the greater response complexity in this transition regime rather than as evidence that the constitutive and kinematic nonlinearities are omitted. The PLA damage evolution and TPU finite-deformation behavior are explicitly resolved in the finite-element simulations used to construct the training dataset. The Transformer does not replace these physical formulations; instead, it approximates the resulting mapping from the aperiodic material layout and strain coordinate to the structural response. Within this surrogate, self-attention captures spatial interactions and load redistribution among different cells, while the strain-conditioned decoder represents the nonlinear dependence of stress on strain. Nevertheless, the larger local RMSE indicates that abrupt damage- and instability-driven transitions remain more difficult to approximate than smooth response segments and therefore represent a remaining limitation of the present surrogate model.

Finally, the test-set predictions in Fig. 3f,g confirm the predictive capability of the surrogate model. Across five repeated training runs, the Transformer achieved an SEA MRE of $4.885 \pm 0.164\%$ with $R^2 = 0.9913 \pm 0.0004$, a peak-force MRE of $8.243 \pm 1.981\%$ with $R^2 = 0.9827 \pm 0.0071$, and a full-curve RMSE of 0.9686 ± 0.0086 MPa. The predicted scalar responses remain closely distributed around the diagonal, supporting the use of the surrogate as an efficient evaluator in the subsequent NSGA-II optimization. The distribution audit in Fig. S3 nevertheless shows that the conventional test set is primarily an in-distribution interpolation test; performance for material-ratio extrapolation is discussed separately below.

A parameter-matched comparison with alternative encoders is summarized in Table S4 in the Supporting Information. No encoder was optimal for every response quantity. The Transformer produced the lowest SEA MRE and full-curve RMSE, whereas the CNN produced the lowest mean peak-force MRE. The Transformer was therefore retained not because of universal superiority, but because it provided the best combined accuracy for SEA and the complete stress–strain response, which are central to the subsequent optimization. In addition, self-attention provides an explicit mechanism for representing non-local interactions between spatially separated material regions. The competitive CNN performance indicates that local spatial correlations also remain highly informative for the present small and regular 4×7 grid.

The learning-curve and extreme-composition tests also clarify the range over which the surrogate can be used reliably. Increasing the training-set size from 500 to 4000 reduced the SEA MRE from 8.147% to 4.885% and the full-curve RMSE from 1.0359 to 0.9686 MPa. From 3000 to 4000 samples, the relative improvements in SEA MRE, peak-force MRE, and full-curve RMSE were 4.73%, 5.69%, and 0.78%, respectively. Thus, the curve metric approached a plateau, but the combined response metrics did not satisfy the predefined full-convergence criterion. When all 169 layouts with $k \le 2$ or $k \ge 26$ were excluded from training and validation and used only as an extrapolation challenge, the SEA MRE, peak-force MRE, and curve RMSE increased to $13.589 \pm 1.766\%$, $15.928 \pm 3.822\%$, and 1.0556 ± 0.0301 MPa, respectively. These results show that optimization candidates approaching extreme material compositions require additional finite-element verification.

3.3. Multi-objective optimization and cluster analysis

The validated surrogate model was subsequently coupled with NSGA-II to maximize SEA and minimize peak impact force over the binary TPU/PLA layout space. Fig. 4 summarizes the optimization workflow, convergence history, resulting Pareto frontier, cluster-level layout characteristics, and validation of representative solutions. The final non-dominated designs were retained for high-fidelity finite-element and experimental assessment.

As shown in Fig. 4b, the hypervolume increases rapidly in the early generations and gradually approaches a plateau, indicating that the NSGA-II search progressively improves the quality of the Pareto front and reaches a stable trade-off boundary. The final optimized solutions form a clear Pareto frontier in the SEA and peak force space, as shown in Fig. 4c, indicating that no single material layout can simultaneously maximize energy absorption and minimize impact force. Instead, improvement in one objective is generally achieved at the expense of the other. Fig. 4d further shows that increasing the TPU ratio tends to shift the solutions toward lower peak force but also lower SEA, revealing an overall trade-off associated with increasing soft-phase content. However, the dispersion of the solutions at similar TPU ratios also suggests that phase fraction alone does not uniquely determine the mechanical performance; rather, the spatial organization of the soft phase plays an equally important role.

To further reveal the intrinsic organization of the optimized solutions, the Pareto set was partitioned into four clusters in the performance space using K-means analysis, as shown in Fig. 4c. These clusters correspond to distinct performance regimes along the Pareto frontier, ranging from low-force/low-SEA solutions to high-SEA/high-force solutions. The TPU frequency maps in Fig. 4f show that each cluster exhibits a different statistical preference for soft-phase placement. Cluster 1 exhibits the highest TPU frequency, with the soft phase broadly distributed and frequently forming continuous horizontal regions. The TPU frequency progressively decreases from Cluster 1 to Cluster 4 as SEA and peak force increase. Cluster 2 retains an interpenetrating PLA/TPU arrangement with a relatively high interface density, whereas Cluster 3 marks the emergence of vertically connected PLA load paths. Cluster 4 contains only sparse TPU regions and is dominated by a continuous PLA load-bearing skeleton. Therefore, the Pareto solutions are not randomly scattered, but instead self-organize into several layout families with distinct structural characteristics.

Representative solutions selected from different clusters were further evaluated by surrogate prediction, direct simulation, and experiment, as shown in Fig. 4e. Good agreement is observed among the three evaluation approaches, indicating that the optimized layouts are not artifacts of the surrogate model and that the surrogate-assisted inverse design framework can identify physically meaningful Pareto-optimal solutions. These results provide the basis for the following analysis of representative designs and their underlying deformation mechanisms.

3.4. Representative Pareto designs and deformation mechanisms

To clarify how different soft–hard organizations govern the trade-off between SEA and peak force, one representative solution was selected from each of Clusters 1–4 for load–displacement and deformation-field analyses. These four designs span the principal performance range of the Pareto frontier. In addition, phase topology was quantified across all Pareto-optimal solutions using directional PLA and TPU connectivity, complete load paths, phase fragmentation, same-phase adjacency, and PLA–TPU interface descriptors. These quantitative measures were used to connect the cluster-level deformation characteristics to the resulting SEA and peak-force responses. The definitions of the topology descriptors, the composition-controlled statistical procedure, and the complete 21-metric results are provided in Section S9 and Table S5 of the Supporting Information.

As shown in Fig. 5a,b, the four representative designs exhibit a clear progression from the low-force/low-SEA response of Cluster 1 to the high-force/high-SEA response of Cluster 4. This progression is consistent with the overall effect of TPU fraction observed in Fig. 4d, but the dispersion among designs with similar TPU fractions indicates that composition alone is insufficient to explain the performance differences. The cluster-level topology metrics in Table 1a provide a quantitative description of the corresponding structural transition. The probability of containing at least one complete TPU horizontal row decreases from 93.9% in Cluster 1 to 42.5% in Cluster 2, 25.5% in Cluster 3, and 0% in Cluster 4. Conversely, the probability of containing at least one complete PLA vertical column increases from 0% in Clusters 1 and 2 to 62.7% in Cluster 3 and 100% in Cluster 4. These results demonstrate a systematic transition from TPU-dominated transverse compliant paths to PLA-dominated vertical load-bearing paths.

The deformation fields in Fig. 5c,d are consistent with the topology statistics in Table 1a. Cluster 1 contains the largest proportion of complete TPU horizontal rows. These transverse compliant regions interrupt direct PLA load-transfer paths and allow deformation to spread progressively across the structure, resulting in relatively low stress concentration and the lowest peak force. However, the absence of complete PLA vertical columns limits the formation of a continuous stiff skeleton,

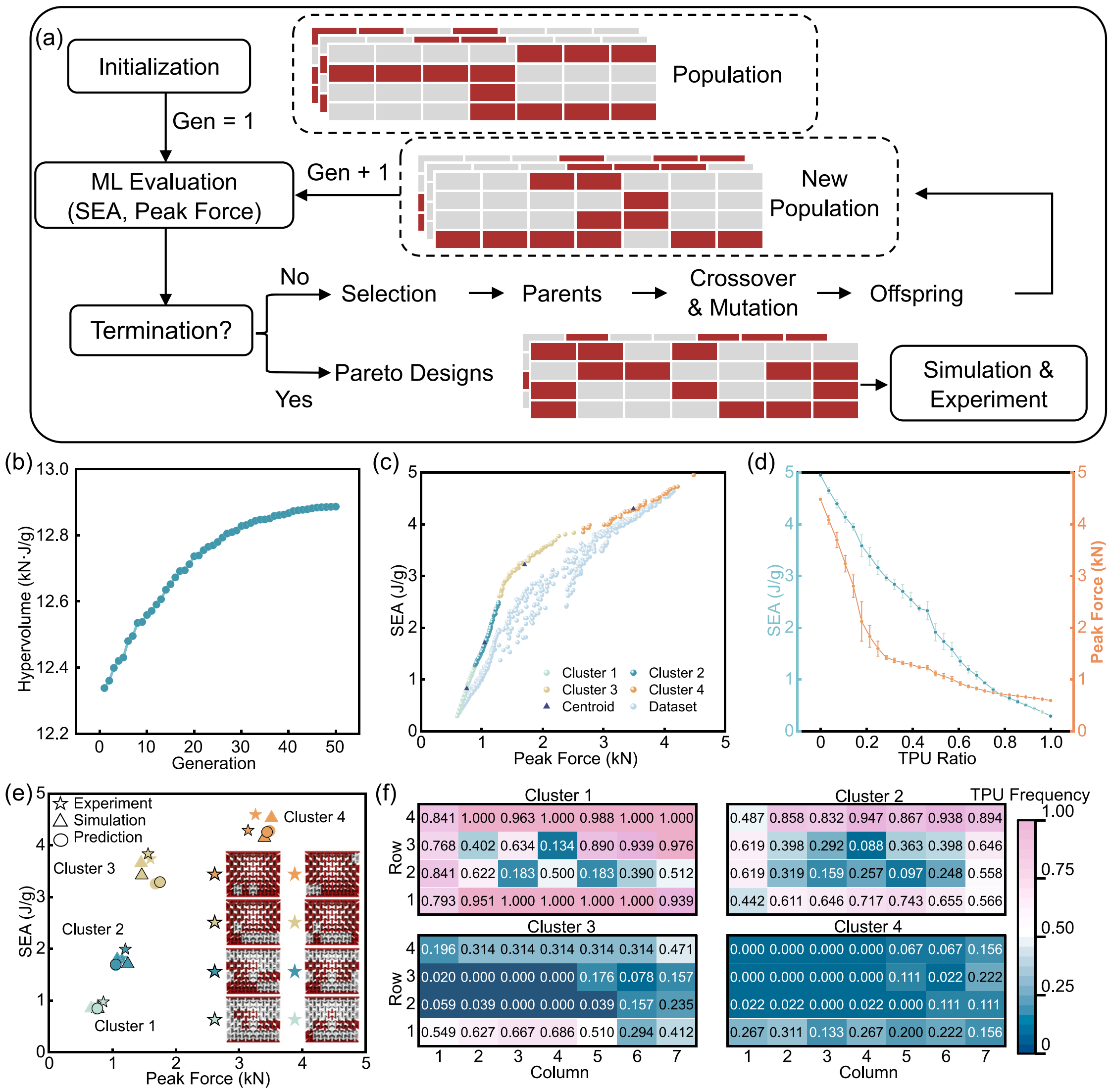

Fig. 4. Multi-objective optimization using NSGA-II and analysis of Pareto-optimal designs. (a) Workflow of the surrogate-assisted optimization framework, where candidate material layouts are iteratively evaluated by the trained model, followed by selection, crossover, and mutation to generate new populations until convergence; the final Pareto designs are further validated by high-fidelity simulations and experiments. (b) Evolution of hypervolume with generation, indicating the convergence behavior and progressive improvement of the Pareto front. (c) Distribution of Pareto-optimal solutions in the SEA–peak-force objective space, colored by clustering results, revealing distinct design families with different trade-off characteristics. (d) Variation of SEA and peak force as a function of TPU ratio, illustrating the intrinsic trade-off governed by soft–hard material composition. (e) Experimental validation of representative designs, with comparison among experiment, simulation, and prediction, demonstrating good agreement and confirming the reliability of the proposed framework. (f) Spatial distribution of TPU frequency within each cluster, highlighting characteristic material layout patterns associated with different performance regimes.

reducing the load sustained during compression and therefore limiting SEA. Cluster 2 retains some TPU horizontal paths but exhibits the highest mean PLA–TPU interface density (0.458). Its interpenetrating topology promotes progressive load redistribution between the two phases, producing a higher sustained load and SEA than Cluster 1 while maintaining a considerably lower peak force than the PLA-dominated clusters.

The deformation fields in Fig. 5e,f show the corresponding transition toward PLA-dominated load transfer. In Cluster 3, 62.7% of the optimized layouts contain at least one complete PLA vertical column. The stress field consequently develops increasingly aligned high-stress regions, indicating that a larger fraction of the compressive load is transferred through continuous PLA paths. In Cluster 4, every analyzed layout contains at least one complete PLA vertical column, while complete TPU horizontal rows are absent. The continuous PLA skeleton supports a higher load level over the compression process, producing the highest SEA. At the same time, direct load transfer through the stiff PLA columns increases the initial compression resistance and therefore the peak force. The deformation fields and topology statistics thus provide mutually consistent evidence for the transition from compliant collapse to stiff-skeleton-dominated load transfer.

Although the cluster-level results establish a clear relationship between topology and performance, some of these differences may arise from the overall TPU fraction. Therefore, arrangement-specific effects were further evaluated after controlling for the exact TPU cell count, as summarized in Table 1b. Complete PLA vertical columns show the strongest positive association with peak force (r = 0.589, q = 0.0012) and are also positively associated with SEA (r = 0.359, q = 0.0012). This quantitatively supports the deformation fields in Fig. 5e,f, where vertically aligned PLA regions act as direct load-bearing paths. In contrast, TPU horizontal orientation is negatively associated with both peak force (r = −0.357, q = 0.0012) and SEA (r = −0.617, q = 0.0012), consistent with the distributed compliant deformation observed in Fig. 5c. TPU fragmentation is positively associated with both responses,

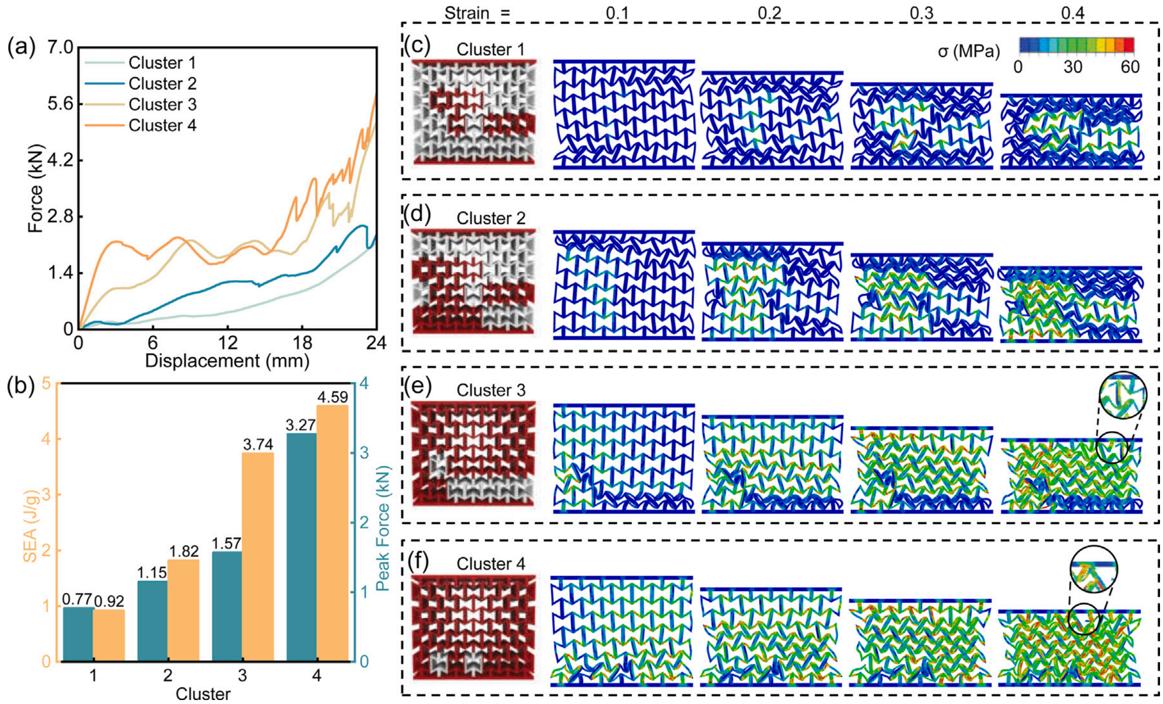

Fig. 5. Mechanical responses and deformation evolution of representative optimized designs selected from different Pareto clusters. (a) Quasi-static load–displacement curves of four representative solutions. (b) Corresponding SEA and peak force of these solutions, highlighting the trade-off progression from low-force/low-SEA to high-SEA/high-force designs. (c–f) Material layouts and simulated von Mises stress distributions of representative designs from Clusters 1–4, respectively, at nominal compressive strains of 0.1, 0.2, 0.3, and 0.4.

Table 1
Quantitative topology characteristics of the four Pareto clusters and their composition-controlled relationships with mechanical performance. Correlations were calculated after controlling for the exact TPU cell count. The q-values were obtained using Benjamini–Hochberg correction of stratified permutation tests.

(a) Cluster-level topology characteristics

Cluster	n	Full TPU row	Full PLA column	Interface density
1	82	93.9%	0.0%	0.342
2	113	42.5%	0.0%	0.458
3	51	25.5%	62.7%	0.228
4	45	0.0%	100.0%	0.136

(b) Composition-controlled topology–performance relationships

Topology metric	r_{force}	q_{force}	r_{SEA}	q_{SEA}
PLA vertical columns	0.589	0.0012	0.359	0.0012
TPU horizontal orientation	−0.357	0.0012	−0.617	0.0012
TPU fragmentation	0.350	0.0031	0.218	0.0063
TPU same-phase adjacency	−0.305	0.0076	−0.197	0.0162
Left–right PLA–TPU interfaces	0.252	0.0012	0.480	0.0012
Top–bottom PLA–TPU interfaces	−0.094	0.0171	−0.359	0.0012

whereas TPU same-phase adjacency is negatively associated with them. Thus, fragmented TPU regions are less effective at interrupting the PLA skeleton, while connected TPU regions provide more effective compliant deformation paths. The complete composition-controlled results for all 21 topology descriptors, including the nonsignificant results, are reported in Table S5 of the Supporting Information.

Taken together, Fig. 4d, Fig. 5, and Table 1 demonstrate that the SEA–peak-force trade-off is governed jointly by material composition and directional phase continuity. The overall TPU fraction determines the broad performance trend, whereas the organization of TPU and PLA controls how the load is redistributed within a given composition. Continuous TPU regions transverse to the loading direction act as compliant deformation paths that suppress peak force, while uninterrupted PLA columns form direct load-bearing paths that increase the sustained load and SEA. The orientation of the PLA–TPU interfaces further determines whether the phases promote lateral load redistribution or interrupt vertical load transfer. These findings provide a physically interpretable design rule: peak-force suppression requires connected compliant paths, whereas high SEA requires sufficient continuity of the PLA skeleton.

3.5. UAV airdrop validation of practical protective performance

To further assess the practical applicability of the proposed design framework, UAV airdrop tests were conducted using protective boxes fabricated with pure PLA, pure TPU, and the optimized multi-material layout. Fig. 6a–c compares the representative landing responses of the pure PLA, pure TPU, and optimized multi-material boxes during free-fall impact from a height of 1.5 m, with the corresponding landing processes provided in Video S1. The pure PLA box shows little visible structural deformation upon ground contact and rebounds immediately after landing, indicating a relatively stiff impact response with limited buffering capability. By contrast, the pure TPU box undergoes much larger deformation, revealing a stronger capacity for deformation-mediated impact attenuation. However, such a highly compliant response is also accompanied by more pronounced elastic recovery after impact. The optimized multi-material box exhibits an intermediate deformation mode, indicating that it combines the buffering effect of the soft phase with the structural support provided by the hard phase. In addition to moderating the initial impact, the optimized box retains a more stable landing posture with limited rebound and rotation. This difference also shows that peak force alone does not fully describe landing performance. Post-impact stability also depends on rebound impulse, recoverable elastic energy, changing contact conditions, and angular momentum.

The practical airdrop configuration is illustrated in Fig. 6d, in which egg payloads were used as representative fragile objects, and the protective box was equipped with an embedded sensing unit. Representative payload-drop outcomes are shown in Fig. 6e–g. For

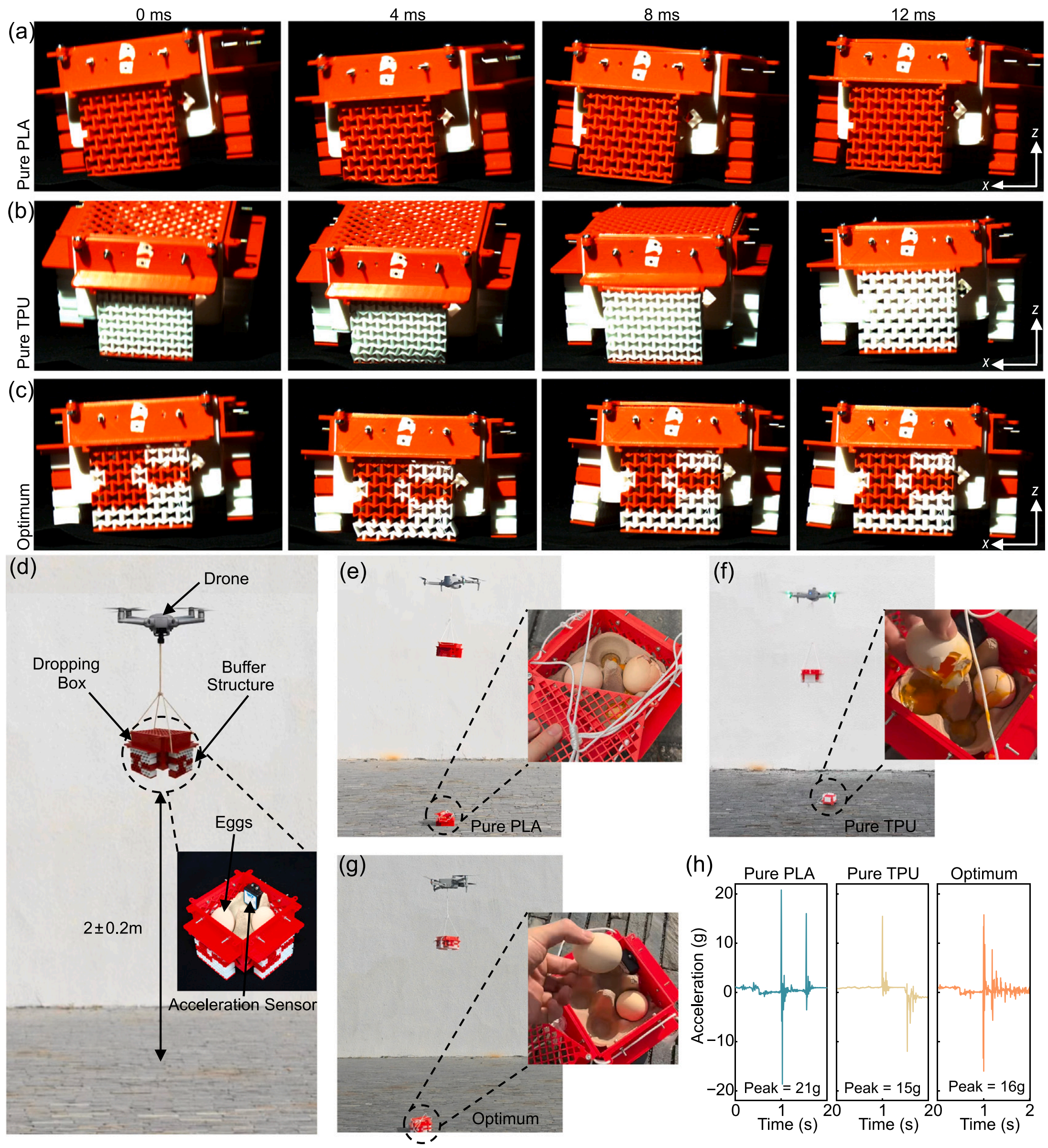

Fig. 6. Application-level validation of the UAV airdrop protective boxes with different material layouts. (a–c) Representative landing snapshots of the boxes with pure PLA, pure TPU, and the optimized multi-material design, respectively, during airdrop from a height of 1.5 m. (d) Schematic of the 2 m payload-protection airdrop test with egg payloads and embedded acceleration sensing. (e–g) Post-impact outcomes for the three designs: the eggs carried by the pure PLA and pure TPU boxes are damaged after landing, whereas the egg protected by the optimized multi-material design remains intact, demonstrating superior impact mitigation capability. (h) Measured payload acceleration histories for the pure PLA, pure TPU, and optimized designs.

the pure PLA box, the structure impacts the ground in a stiff manner with limited visible deformation, so that the impact load is transferred rapidly to the payload, leading to fracture of the raw eggs after landing. For the pure TPU box, the pronounced deformation reduces the initial impact response, but the subsequent release of recoverable elastic energy produces strong rebound and overturning. By contrast, the optimized multi-material box exhibits a more stable landing response: the TPU regions accommodate impact deformation, while the PLA skeleton restricts excessive elastic recovery and maintains the load-bearing geometry during ground contact. Consequently, rebound-induced rotation is suppressed, and the egg payload remains intact without visible cracks or breakage (Fig. 6g, Video S2). These results show that the optimized soft–hard layout provides not only impact attenuation but also improved post-impact stability under realistic aerial-delivery conditions.

The measured payload acceleration histories are compared in Fig. 6h. The pure PLA box produces the highest peak acceleration of 21 g because its stiff structure transfers the impact load more directly to the payload. The pure TPU box gives the lowest value of 15 g, whereas the optimized design exhibits an intermediate peak of 16 g. However, the lower acceleration of the pure TPU box does not result in better overall landing performance because its large recoverable deformation generates substantial rebound and rotational motion. The optimized box instead maintains a stable landing posture by combining deformation-mediated buffering with structural constraint from the PLA skeleton.

This distinction clarifies the relationship between the numerical optimization and the UAV airdrop experiment. The simulated peak-force objective characterizes the maximum instantaneous transmitted load under a controlled impact condition, whereas stable landing additionally depends on post-impact rebound and rotation. These kinematic responses were not explicitly included in the present optimization but were assessed through the application-level airdrop tests. Therefore, the

16 g response of the optimized design represents a more balanced compromise between impact attenuation and post-impact stability rather than the minimum acceleration alone. Future application-specific optimization may further incorporate rebound height, maximum tilt angle, angular velocity, or settling time as additional objectives or constraints.

Overall, the UAV airdrop experiments demonstrate that the optimized multi-material design achieves a favorable balance among impact attenuation, rebound suppression, landing stability, and payload integrity. The results complement the simulated peak-force optimization and confirm the practical value of the proposed inverse-design strategy for fragile-payload delivery under unconstrained landing conditions.

4. Conclusions

A surrogate-assisted inverse-design framework was developed for non-periodic multi-material energy-absorbing metamaterials intended for UAV airdrop protection. Fracture-aware finite-element simulations, a Transformer-based dual-response surrogate, and NSGA-II were integrated to explore the combinatorial design space generated by cell-wise TPU/PLA assignment within a fixed re-entrant lattice. The effective constitutive framework was assessed using pure-PLA, pure-TPU, and multi-material structures under quasi-static compression and impact loading. In particular, progressive PLA damage was found to be necessary because an elastic–plastic description alone retained excessive post-yield load-carrying capacity and consequently overestimated SEA and peak impact force. When the damage-initiation strain and failure displacement were independently perturbed by $\pm 20\%$, the resulting SEA changes remained between −0.38% and +5.33%, while the peak-force changes remained between −0.55% and +0.63%, indicating that the predicted global responses were reasonably robust within the investigated parameter range.

Accurate in-distribution predictions were obtained using the trained Transformer surrogate. Across five repeated training runs, an SEA MRE of $4.885 \pm 0.164\%$, a peak-force MRE of $8.243 \pm 1.981\%$, and a full-curve RMSE of 0.9686 ± 0.0086 MPa were achieved. The surrogate-assisted optimization produced a well-defined Pareto frontier spanning low-force/low-SEA to high-force/high-SEA responses, thereby demonstrating that the competing objectives could be systematically balanced through structural-scale material organization. The strain-dependent loss was found to be particularly important for retaining the initial stiffness, load-path establishment, and collapse-onset characteristics that govern the subsequent energy-absorbing response. However, the increased RMSE in the intermediate-strain regime also showed that abrupt damage- and instability-driven transitions remain more difficult to reconstruct than smoother response segments.

The performance trade-off was shown to be governed jointly by material composition and directional phase continuity rather than by TPU fraction alone. Connected TPU regions oriented transverse to the loading direction formed compliant deformation paths, promoted progressive collapse, and reduced peak force. Conversely, uninterrupted PLA columns provided direct load-bearing paths, increased the sustained compressive load, and enhanced SEA, although a higher impact-force peak was consequently produced. Intermediate Pareto solutions were obtained when sufficient PLA skeleton continuity was retained while deformation and load redistribution were accommodated by connected TPU regions. A physically interpretable design principle was therefore established: peak-force suppression requires continuous compliant paths, whereas high SEA requires adequate continuity of the stiff load-bearing skeleton.

The practical relevance of the optimized layout was further assessed through quasi-static compression, drop-weight impact, and UAV airdrop experiments. During the 2 m payload-protection airdrop tests, peak payload accelerations of 21 g, 15 g, and 16 g were measured for the pure PLA, pure TPU, and optimized multi-material boxes, respectively. Although the pure TPU box produced the lowest instantaneous acceleration, substantial elastic recovery caused pronounced rebound and overturning, and the payload was damaged. In contrast, the optimized box combined deformation-mediated buffering with structural constraint from the PLA skeleton, thereby suppressing excessive rebound and maintaining a stable landing posture. The egg payload protected by the optimized design remained intact, whereas those carried by the two single-material boxes were damaged. These results demonstrate that practical protective performance is governed by the combined effects of impact attenuation, irreversible energy dissipation, load support, and post-impact stability rather than by minimization of the instantaneous acceleration or force peak alone.

Several limitations of the present framework are acknowledged. The numerical models were established under a two-dimensional plane-strain assumption, and perfect bonding was assumed at the TPU/PLA interfaces. Effective constitutive properties were calibrated at the structural level; therefore, printing-induced porosity, anisotropy, interlayer defects, and stochastic interfacial imperfections were not represented explicitly. In addition, the dynamic dataset and optimization were constructed for a single impact energy of 5 J and an initial velocity of 2000 mm/s. Because multi-rate material-level test data were unavailable, a rate-independent effective formulation was adopted for PLA. The quasi-static compression experiments were also conducted under monotonic loading without a controlled unloading stage. Consequently, the nonlinear unloading path, residual deformation, post-unloading stability, including possible delayed collapse after load removal, and repeated-loading capability were not quantified. Although the optimized protective box retained its overall integrity immediately after the single UAV airdrop test, this observation does not establish complete structural recovery or reusability. The conventional test set primarily assessed interpolation within the sampled material-composition range, while substantially larger errors were observed in the extreme-composition extrapolation challenge. Furthermore, only SEA and peak impact force were included as optimization objectives, whereas rebound, rotation, settling time, repeated-impact performance, and payload-specific constraints were assessed only through application-level experiments or were not explicitly considered.

Future work should first address the main modeling limitations identified here, including three-dimensional effects, TPU/PLA interface behavior, FDM-induced defects and anisotropy, and strain-rate dependence. Extending the training data to multiple impact energies, velocities, orientations, and repeated-loading conditions would allow the optimization to target robustness rather than a single prescribed impact case. Controlled unloading and cyclic tests are also needed to quantify recovery, residual deformation, and reusability. For application-level design, rebound height, tilt angle, angular velocity, settling time, and payload acceleration could be introduced as additional objectives or constraints. Uncertainty-aware active learning could then be used to add high-fidelity simulations where the surrogate is least reliable.

CRediT authorship contribution statement

Shitong Fang: Writing – review & editing, Writing – original draft, Visualization, Validation, Supervision, Software, Resources, Project administration, Methodology, Investigation, Funding acquisition, Formal analysis, Data curation, Conceptualization. **Haobin Lin:** Writing – review & editing, Writing – original draft, Visualization, Validation, Methodology, Investigation, Formal analysis, Data curation. **Aipeng Ye:** Validation, Methodology, Investigation, Data curation. **Zhihui Lai:** Validation, Supervision, Investigation. **Haitao Ye:** Writing – review & editing, Validation, Methodology, Investigation, Formal analysis. **Qiang Gao:** Investigation, Formal analysis. **Mingjing Cai:** Writing – original draft, Methodology, Investigation. **Xiaoya Zhai:** Writing – review & editing, Validation, Methodology, Formal analysis. **Xiaohao Sun:** Validation, Methodology, Formal analysis. **Liuchao Jin:** Writing – review & editing, Writing – original draft, Visualization, Validation, Supervision, Project administration, Methodology, Investigation, Formal analysis, Data curation, Conceptualization. **Wei-Hsin Liao:** Writing – review & editing, Supervision, Resources, Investigation, Funding acquisition, Conceptualization.

Declaration of competing interest

The authors declare that they have no known competing financial interests or personal relationships that could have appeared to influence the work reported in this paper.

Acknowledgments

S.F. acknowledges support by National Natural Science Foundation of China (Grant No. 52575130), Guangdong Basic and Applied Basic Research Foundation (Grant No. 2026A1515010148), and Shenzhen Natural Science Fund (Grant No. JCYJ20230808105206013). W.-H.L. acknowledges support by Hong Kong Research Grants Council (SRFS2627-4S01 and STG5/E-103/24-R), and the Hong Kong Centre for Logistics Robotics of InnoHK. L.J. acknowledges support by the Hong Kong Research Grants Council under the Hong Kong PhD Fellowship Scheme (No. PF21-60853).

Appendix A. Supplementary data

Supplementary material related to this article can be found online at https://doi.org/10.1016/j.ijmecsci.2026.112110.

Data availability

All data supporting the findings of this study are included within the article.

References

[1] Zadpoor AA. Mechanical meta-materials. Mater Horizons 2016;3(5):371–81.
[2] Bertoldi K, Vitelli V, Christensen J, Van Hecke M. Flexible mechanical metamaterials. Nat Rev Mater 2017;2(11):1–11.
[3] Jiao P, Mueller J, Raney JR, Zheng XR, Alavi AH. Mechanical metamaterials and beyond. Nat Commun 2023;14(1):6004.
[4] Lakes R. Foam structures with a negative Poisson's ratio. Science 1987;235(4792):1038–40.
[5] Yin H, Zhang W, Zhu L, Meng F, Liu J, Wen G. Review on lattice structures for energy absorption properties. Compos Struct 2023;304:116397.
[6] Wang W-J, Yang H, Zhang W-M, Shang N, Ma L. Experimental study on the impact resistance of fill-enhanced mechanical metamaterials. Int J Mech Sci 2025;285:109799.
[7] Meng L, Zhong M, Gao Y, Gao T, Hou Y, Zhu J, Breitkopf P, Zhang W. Impact resisting mechanism of tension–torsion coupling metamaterials. Int J Mech Sci 2024;272:109100.
[8] Liu J, Bao B, Chen J, Wu Y, Wang Q. Marine energy harvesting from tidal currents and offshore winds: A 2-DOF system based on flow-induced vibrations. Nano Energy 2023;114:108664.
[9] Dong P, Ding W, Yuan H, Wang Q. 3D-printed polymeric lattice-enhanced sustainable municipal solid waste incineration fly ash alkali-activated cementitious composites. Dev Built Environ 2022;12:100101.
[10] Song M, Wang YQ, Li Y, Wang Q. A reconfigurable mechanical structure inspired by the mechanism of Rubik's cube: Design, analysis and experiment. Eng Struct 2025;343:121275.
[11] Liu Q, Xiong J, Lin W, Liu J, Wan Y, Guo CF, Wang Q, Liu Z. Porous polymers: structure, fabrication and application. Mater Horizons 2025;12(8):2436–66.
[12] Zhang K, Jiang J, Jin L, Gao Q, Zhai X, Zhou S, Li Z, Li J, Liao W-H. Low-melting-point alloy/polyurethane auxetic composite foam for outstanding impact protection with favorable shape memory effect. Smart Mater Struct 2025;34(4):045025.
[13] Zhang K, Gao Q, Jiang J, Chan M, Zhai X, Jin L, Zhang J, Li J, Liao W-H. High energy dissipation and self-healing auxetic foam by integrating shear thickening gel. Compos Sci Technol 2024;249:110475.
[14] Xu W, Zhang M, Xu H, Yu M, Jin L, Zhai X, Jiang J. INPR-Connector: Interlocking negative Poisson's ratio connectors design for deployable energy absorption structures. Compos Part B: Eng 2025;297:112243.
[15] Wu S, Wang R, Jin L, Huang X, Li W, Zhou K, Ge Q. Digital light processing 3D printing of large-scale and crack-free ceramics with perforated internal honeycomb structures. Virtual Phys Prototyp 2025;20(1):e2589472.
[16] Wang D. Impact behavior and energy absorption of paper honeycomb sandwich panels. Int J Impact Eng 2009;36(1):110–4.
[17] Cáceres-Naranjo D, Bernad C, Calvo S, Royo J. Assessment and modelling of corrugated board dynamic properties under impact loads. Application to edge crush disposition. Results Eng 2023;18:101072.
[18] Xi H, Guo C, Yang J, Wang X, Wang B, Huang S, Wang Z. Cushioning performance of a novel polyurethane foam material applied in fragile packaging. Acta Mech Solida Sin 2024;37(3):487–97.
[19] Li D, Zhang G, Wu M, Lin L, Liu H, Shi J, Lu J, Wang D, Yang Y, Du K. Buffering performance of 3D-printed TPU-based packaging: Experimental and numerical analysis. Mech Res Commun 2025;104492.
[20] Xu W, Wang D, Zhang J, Hu J, Xu H, Jin L, Ye H, Zhao H, Liao W-H. Enhanced energy absorption in re-entrant honeycombs via elliptical double-arrow hybrid design. Thin-Walled Struct 2026;230:115252.
[21] Wang J, Jin L, Gao Q, Liao W-H. Graded infill design of thin-walled structures with connectable nonuniform microstructures based on the data-driven surrogate model. Thin-Walled Struct 2026;231:115426.
[22] Yao S, Zhou H, Gao T, Chen F, Wang Z, Liu K. Origami-inspired highly impact-resistant metamaterial with loading-associated mechanism and localization mitigation. Int J Mech Sci 2025;290:110114.
[23] Cai Y, Wang Z, Liu G, Qian H, Jiang Y. Dual-functional quasi-zero stiffness metamaterial for vibration isolation and impact attenuation. Int J Mech Sci 2025;300:110418.
[24] Zhang X, Yin J, Wu J, Zhao Z, He Z, Yu D, Wen J. Pre-torsion tubular metamaterials for low-frequency vibration attenuation and impact resistance. Int J Mech Sci 2025;110915.
[25] He Y, Lu G, Wang T, Wang L, Tse KM. Optimized hexagonal perforated honeycomb–chiral metamaterial for multidirectional energy absorption. Int J Mech Sci 2025;301:110521.
[26] Choudhry NK, Panda B, Dixit US. Energy absorption characteristics of fused deposition modeling 3D printed auxetic re-entrant structures: A review. J Mater Eng Perform 2023;32(20):8981–99.
[27] Yan J, Gao Y, Xiang S, Zhan J, Jin L, Huang H. A strategy for 3D printed Al-based bi-material lattice optimization: Thermal-mechanical coupling performance with load-bearing and energy-absorption. Adv Funct Mater 2026;36(20):e21424.
[28] Ye H, Huang X, Jin L, Zhou S, Xie G, Hu Z, Li R, Mo H, Fang S, Liao W-H, Ge Q, Song X. Multi-material 3D printed compression-induced stretching lattice metamaterials with superior reusable energy absorption. Virtual Phys Prototyp 2026;21(1):e2637380.
[29] Yang H, Zhang J, Wang J, Hu J, Wu Z, Pan F, Wu J. Delocalized deformation enhanced reusable energy absorption metamaterials based on bistable tensegrity. Adv Funct Mater 2025;35(5):2410217.
[30] Khatri NR, Egan PF. Energy absorption of 3D printed ABS and TPU multimaterial honeycomb structures. 3D Printing and Additive Manufacturing 2024;11(2):840–50.
[31] Qi C, Jiang F, Yang S. Advanced honeycomb designs for improving mechanical properties: A review. Compos Part B: Eng 2021;227:109393.
[32] Nazir A, Gokcekaya O, Billah KMM, Ertugrul O, Jiang J, Sun J, Hussain S. Multi-material additive manufacturing: A systematic review of design, properties, applications, challenges, and 3D printing of materials and cellular metamaterials. Mater Des 2023;226:111661.
[33] Mirzaali MJ, Caracciolo A, Pahlavani H, Janbaz S, Vergani L, Zadpoor A. Multi-material 3D printed mechanical metamaterials: Rational design of elastic properties through spatial distribution of hard and soft phases. Appl Phys Lett 2018;113(24).
[34] Yavas D, Liu Q, Zhang Z, Wu D. Design and fabrication of architected multi-material lattices with tunable stiffness, strength, and energy absorption. Mater Des 2022;217:110613.
[35] Zhi Q, Li D, Sun H, Zhu W. Adjustment of multi-directional elastic properties of chiral metamaterial via a 3D printing-based soft-hard bi-material strategy. Compos Struct 2023;307:116646.
[36] Ye H, Li C, Yu S, Li H, Lian Y, He X, Chen J, Huang X, Jin L, Cheng J, Wang R, Huang L, Zhang B, Song X, Lu Y, Ge Q. Adaptive energy dissipator with compression-to-tension design. Adv Funct Mater 2026;36(19):e21393.
[37] Bian Z, Gong Y, Sun Z, Zhao L, Zhang J, Hu N. Design and energy absorption characteristics of a novel honeycomb with embedded chiral structures. Compos Struct 2024;333:117944.
[38] Cui C, Chen T, Qiao Y, Kuang X, Hua L, Cui X, Yan H. Deformation response and enhanced energy absorption capacity of a novel re-entrant honeycomb with hybrid structures and bi-material under in-plane compression. Compos Struct 2025;367:119268.
[39] Zhang D, Li H, Chen C, Wu C, Wu C, Li Q, Fang J. Enhancing performance and reusability of multi-material honeycomb metamaterials via blended FDM. Int J Mech Sci 2026;111436.
[40] Satpati A, Maurizi M, Yao D, Kim S, Wu HF, Lee EC, Zheng XR. Multi-objective automatic discovery of optimized metamaterials for varying velocity impact protection. Mater Des 2025;258:114657.
[41] Zhang H, Chen P, Lin G, Sun W. A corrugated gradient mechanical metamaterial: Lightweight, tunable auxeticity and enhanced specific energy absorption. Thin-Walled Struct 2022;176:109355.
[42] Ding J, Wen Y, Wang Q, Qu S, Song X, Zhang B. Material-gradient enabled enhancement of strength and strain-hardening of lattice structures. Adv Sci 2025;12(48):e11185.
[43] Liu Q, Liu Y, Shi J, Liu Z, Wang Q, Guo CF. High-porosity foam-based iontronic pressure sensor with superhigh sensitivity of 9280 kPa^{-1}. Nano-Micro Lett 2022;14(1):21.

[44] Wu X, Zhang S, Ding L, Wu W, Ma Y, Deng Z. Bi-material multistable auxetic honeycombs with reusable and enhanced energy-absorbing phases under in-plane crushing. Thin-Walled Struct 2024;201:111988.
[45] Chen S, Tan X, Hu J, Wang B, Wang L, Zou Y, Wu L. Continuous carbon fiber reinforced composite negative stiffness mechanical metamaterial for recoverable energy absorption. Compos Struct 2022;288:115411.
[46] Hua J, Zhou Y, Chen CQ. Design and analysis of a tunable multistable mechanical metamaterial. Int J Mech Sci 2024;272:109170.
[47] Lei Y, Wang Y, Cui R, Huang X, Zhang L, Jin Y, Gao J, Deng B. 3D hyperbolic kirigami metamaterials with tunable auxeticity and multistability. Adv Sci 2025;12(35):e06703.
[48] Chen S, Lian X, Zhu S, Li M, Wang B, Wu L. A re-usable negative stiffness mechanical metamaterial composed of bi-material systems for high energy dissipation and shock isolation. Compos Struct 2023;322:117366.
[49] Wang R, Niu B, Yang R. Generalizable design of composite multistable honeycomb structures with tailored morphing. Int J Mech Sci 2025;110586.
[50] Pan Y, Zhou Y, Wang M, Gao Q, Sun B. A novel reinforced cylindrical negative stiffness metamaterial for shock isolation: analysis and application. Int J Solids Struct 2023;279:112391.
[51] Ma WWS, Yang H, Zhao Y, Li X, Ding J, Qu S, Liu Q, Hu Z, Li R, Tao Q, et al. Multi-physical lattice metamaterials enabled by additive manufacturing: design principles, interaction mechanisms, and multifunctional applications. Adv Sci 2025;12(8):2405835.
[52] Zhu S, Wang B, Tan X, Hu J, Wang L, Zhou Z, Chen S. A novel bi-material negative stiffness metamaterial in sleeve-type via combining rigidity with softness. Compos Struct 2021;262:113381.
[53] Tan X, Cao B, Liu X, Zhu S, Chen S, Kadic M, Wang B. Negative stiffness mechanical metamaterials: a review. Smart Mater Struct 2025;34(1):013001.
[54] Guan Y, Zhang X, Cao X, Yang H, Wang S, Cao W, He C. Dual-material TPMS metamaterial with high load-bearing capacity and performance stability. Int J Mech Sci 2025;110613.
[55] He Y, Yang H, Zhang C, Liu W, Wang L, Wang T, Lu G, Yu J, Tse KM. Energy absorption and deformation of re-entrant bi-material tubular metamaterials. Int J Mech Sci 2026;111495.
[56] Cheng Q, Yin J, Wen J, Yu D, Tan VB, Zhai W. Deformation control and energy absorption enhancement by hierarchical dual-phase design. Int J Mech Sci 2025;294:110257.
[57] Zhou S, Jin L, Xie G, Zhang K, Gao Q, Liao W-H. Thermally driven reusable dual-phase honeycombs with enhanced mechanical properties. Int J Mech Sci 2026;326:111900.
[58] Wu X, Wang S, Ma Y, Deng Z. Design of mechanical metamaterials with multiple stable stress plateaus. Mech Adv Mater Struct 2024;31(6):1348–65.
[59] Zeng Q, Zhao Z, Lei H, Wang P. A deep learning approach for inverse design of gradient mechanical metamaterials. Int J Mech Sci 2023;240:107920.
[60] Peng B, Wei Y, Qin Y, Dai J, Li Y, Liu A, Tian Y, Han L, Zheng Y, Wen P. Machine learning-enabled constrained multi-objective design of architected materials. Nat Commun 2023;14(1):6630.
[61] Wan X-H, Zhang Y, Guo Q-H, Zheng L-Y. Deep learning-based inverse design of irregular phononic crystals. Int J Mech Sci 2025;297:110335.
[62] Jin L, Zhai X, Jiang J, Zhang K, Liao W-H. Optimizing stimuli-based 4D printed structures: a paradigm shift in programmable material response. In: Sensors and Smart Structures Technologies for Civil, Mechanical, and Aerospace Systems 2024, vol. 12949, SPIE; 2024, p. 321–32.
[63] Chen C-T, Gu GX. Generative deep neural networks for inverse materials design using backpropagation and active learning. Adv Sci 2020;7(5):1902607.
[64] Lin W, Jin L, Jiang Z, Cai M, Lai Z, Yurchenko D, Yan B, Zhou S, Novoselov KS, Liao W-H, Fang S. Machine learning-based inverse design for functional materials: Methods, challenges, and engineering applications. Adv Funct Mater 2026;e75070.
[65] Shen M, Liu K, Mao S, Daraio C. Self-supervised AI for decoding and designing disordered metamaterials. Sci Adv 2026;12(1):eadx7389.
[66] Wei Z, Chen J, Wei K. Generative deep learning for designing irregular metamaterials with programmable nonlinear mechanical responses. Int J Mech Sci 2025;291:110123.
[67] Xiang Y, Hou J, Chen X, Tang K, Wang X. Decoupled design of hybrid mechanical metamaterials via ensembled deep learning. Int J Mech Sci 2025;301:110514.
[68] Gu GX, Chen C-T, Buehler MJ. De novo composite design based on machine learning algorithm. Extrem Mech Lett 2018;18:19–28.
[69] Pahlavani H, Amani M, Saldívar MC, Zhou J, Mirzaali MJ, Zadpoor AA. Deep learning for the rare-event rational design of 3D printed multi-material mechanical metamaterials. Commun Mater 2022;3(1):46.
[70] Zhang H, Luo Y, Kang Z. Bi-material microstructural design of chiral auxetic metamaterials using topology optimization. Compos Struct 2018;195:232–48.
[71] Liang K, Wei Z, Zhang X. Machine learning based inverse design of variable stiffness mechanical metamaterials. Int J Mech Sci 2026;111265.
[72] Peng X-L, Xu B-X. Data-driven inverse design of composite triangular lattice structures. Int J Mech Sci 2024;265:108900.
[73] Liu H, Chen K, Li J, Kang G. Genetic algorithm-based inverse design of symmetry-broken re-entrant honeycomb. Int J Mech Sci 2025;307:110983.
[74] Jin L, Yu S, Cheng J, Ye H, Zhai X, Jiang J, Zhang K, Jian B, Bodaghi M, Ge Q, Liao W-H. Machine learning-driven forward prediction and inverse design for 4D printed hierarchical architecture with arbitrary shapes. Appl Mater Today 2024;40:102373.
[75] Jin L, Yu S, Cheng J, Liu Z, Zhang K, Zhou S, He X, Xie G, Bodaghi M, Ge Q, Liao W-H. Machine learning powered inverse design for strain fields of hierarchical architectures. Compos Part B: Eng 2025;299:112372.
[76] Zolfagharian A, Jin L, Ge Q, Liao W-H, Díaz Lantada A, Franco Martínez F, Zhang T, Liu T, Wang CCL, Mosallanejad MH, Ghanavati R, Saboori A, De Blas-De Miguel A, Solórzano-Requejo W, Cai Y, Dong X, Qu H, Samadiani N, Huang G, Downey A, Fu Y, Yuan L, Lee T-KG, Baniya AA, Waseem E, Sani AR, Kouzani AZ, Wu Y, Nemitz MP, Shirzad M, Oh D, Nam SY, Bonatti AF, Chiesa I, Fortunato GM, Vozzi G, De Maria C, Bodaghi M. Roadmap on artificial intelligence-augmented additive manufacturing. Adv Intell Syst 2026;8(4):e202500484.
[77] Li D, Gao R, Dong L, Lam W-K, Zhang F. A novel 3D re-entrant unit cell structure with negative Poisson's ratio and tunable stiffness. Smart Mater Struct 2020;29(4):045015.
[78] Li B, Deng B, Shou W, Oh T-H, Hu Y, Luo Y, Shi L, Matusik W. Computational discovery of microstructured composites with optimal stiffness-toughness trade-offs. Sci Adv 2024;10(5):eadk4284.
[79] Ha CS, Yao D, Xu Z, Liu C, Liu H, Elkins D, Kile M, Deshpande V, Kong Z, Bauchy M, et al. Rapid inverse design of metamaterials based on prescribed mechanical behavior through machine learning. Nat Commun 2023;14(1):5765.
[80] Bastek J-H, Kochmann DM. Inverse design of nonlinear mechanical metamaterials via video denoising diffusion models. Nat Mach Intell 2023;5:1466–75.
[81] Zou Z, Liu J, Gao K, Chen D, Yang J, Wu Z. Inverse design of functionally graded porous structures with target dynamic responses. Int J Mech Sci 2024;280:109530.
[82] Gao Z, Zhang X, Wu Y, Pham M-S, Lu Y, Xia C, Wang H, Wang H. Damage-programmable design of metamaterials achieving crack-resisting mechanisms seen in nature. Nat Commun 2024;15(1):7373.
[83] Yousefi-Nooraie R, Razavi N, Berto F, Guagliano M, Bagherifard S. Inverse multi-objective design of three-dimensional plate-based heterogeneous mechanical metamaterials. Int J Mech Sci 2026;312:111253.
[84] Ang K, Qiu J, Su B, Li Z, Yao X, Wang Z, Shu X. Deep learning-based inverse design of programmable disordered metamaterials. Int J Mech Sci 2025;110712.
[85] Zhang X-c, Song Z-y, Li Y-n, Xiao L-j, Xu Z, Rao L-x, Ci T-j, Hui X-L. Generative inverse design of metamaterials with customized stress-strain response. Int J Mech Sci 2025;110875.
[86] Rao L, Zhou Y, Liu W, Han H, Qi F, Liu H, Wang S, Zhao J, Zhang Y, Zhang X. Machine-learning-assisted design of re-entrant honeycomb metamaterials with tunable mechanical properties. Int J Mech Sci 2025;305:110778.
[87] Wu D, Xu Z, Wu E, Yuan Z, Dizhi G, Zhang Z. Machine learning-driven customizable mechanical design of diamond plate lattice metamaterials. Int J Mech Sci 2026;310:111140.
[88] Tang M, Wang L, Xin Z, Luo Z. High energy absorption design of porous metals using deep learning. Int J Mech Sci 2024;282:109593.
[89] Zhou S, Zhang K, Jin L, Gao Q, Liao W-H. Efficient data driven optimization framework for designing B-spline honeycombs with excellent energy absorption. Thin-Walled Struct 2025;209:112941.
[90] Wu Z, Xi Z, Li Y, Xiang X, Li R. Dynamic impact characteristics of airdrop cushioning materials and a C- σm curve-based cushioning pad design method. Materials 2026;19(12):2526.
[91] Dong X, Tian Z, Tian K, Liu H, Tang Y, Xiao Y. Analysis of load reduction performance of the honeycomb paperboard cushioning device during the drop process of airdrop unit. Equip Environ Eng 2025;22(6):1–11.
[92] Hooputra H, Gese H, Dell H, Werner H. A comprehensive failure model for crashworthiness simulation of aluminium extrusions. Int J Crashworthiness 2004;9(5):449–64.
[93] Avalle M, Belingardi G, Montanini R. Characterization of polymeric structural foams under compressive impact loading by means of energy-absorption diagram. Int J Impact Eng 2001;25(5):455–72.
[94] Vaswani A, Shazeer N, Parmar N, Uszkoreit J, Jones L, Gomez AN, Kaiser Ł, Polosukhin I. Attention is all you need. Adv Neural Inf Process Syst 2017;30.
[95] Deb K, Pratap A, Agarwal S, Meyarivan T. A fast and elitist multi-objective genetic algorithm: NSGA-II. "IEEE Trans Evol Computation" 2002;6(2):182–97.
[96] Virtanen P, Gommers R, Oliphant TE, Haberland M, Reddy T, Cournapeau D, Burovski E, Peterson P, Weckesser W, Bright J, et al. Scipy 1.0: fundamental algorithms for scientific computing in Python. Nature Methods 2020;17(3):261–72.